

A novel pyramidal cell type promotes sharp-wave synchronization in the hippocampus

David L. Hunt ^{1*}, Daniele Linaro ^{1,2}, Bailu Si ^{1,3}, Sandro Romani ¹ and Nelson Spruston ^{1*}

To support cognitive function, the CA3 region of the hippocampus performs computations involving attractor dynamics. Understanding how cellular and ensemble activities of CA3 neurons enable computation is critical for elucidating the neural correlates of cognition. Here we show that CA3 comprises not only classically described pyramid cells with thorny excrescences, but also includes previously unidentified ‘athorny’ pyramid cells that lack mossy-fiber input. Moreover, the two neuron types have distinct morphological and physiological phenotypes and are differentially modulated by acetylcholine. To understand the contribution of these athorny pyramid neurons to circuit function, we measured cell-type-specific firing patterns during sharp-wave synchronization events in vivo and recapitulated these dynamics with an attractor network model comprising two principal cell types. Our data and simulations reveal a key role for athorny cell bursting in the initiation of sharp waves: transient network attractor states that signify the execution of pattern completion computations vital to cognitive function.

Storage and retrieval of memory engrams in the hippocampus fundamentally relies on the computations of pattern separation and pattern completion^{1–6}. The circuitry thought to implement these computations are the dentate gyrus (DG) and area CA3. The DG orthogonalizes incoming cortical representations (pattern separation) and relays these separated patterns to distinct ensembles in CA3 via the mossy-fiber projection^{7,8}. Once ensemble activity of CA3 cells drives synaptic plasticity between connected members (auto-association), partial cues can reactivate the full representation (pattern completion)¹. The ability of the CA3 network to re-instantiate previously stored representations based on incomplete information is endowed by recurrent circuitry and attractor dynamics^{2,9–11}. This paradigm is the theoretical foundation upon which our understanding of the computational processes involved in hippocampal memory function has been built^{6,12–15}; however, little mechanistic information is available concerning the neural implementation of these processes.

The principal constituents of the CA3 recurrent network are traditionally characterized as a monolithic pyramidal cell population classified by the iconic presence of the postsynaptic specializations of mossy-fiber synapses (thorny excrescences)¹⁶. This anatomical signature implies strong input from the DG, enabling separated patterns to be reliably transferred to the CA3 recurrent network^{7,8,17,18}. Despite the importance of the mossy fiber-to-CA3 connection for the computational processes ascribed to the DG and CA3 regions, several reports have revealed pronounced functional heterogeneity within CA3^{19–23}, which, together with evidence for anatomical heterogeneity²⁴ indicates that the cellular uniformity implicit in the theoretical paradigm should be revised to account for phenotypic diversity of pyramidal neurons and potentially unique circuit motifs^{1,25}.

Throughout the brain, cellular populations initially considered to be homogeneous have been shown to be comprised of distinct cell types with specific circuit structure and function when investigated at sufficient resolution^{26–28}. We explored cellular heterogeneity in CA3 and identified two distinct types of pyramidal cells, which

differed morphologically, physiologically, and synaptically. This observation raises compelling questions regarding the roles for the two types of pyramidal neurons during hippocampus-dependent memory functions. Therefore, we measured pyramidal cell spiking dynamics during sharp waves (SWs) in vivo, because SWs represent spontaneous replay of ensemble dynamics critical to hippocampal memory function²⁹. We analyzed the cell-type-specific contributions to these events to gain insight into the attractor dynamics that implement pattern completion in area CA3. To relate the cell-type-specific activity patterns we observed experimentally to the computations implemented by attractor dynamics, we simulated neural synchronization dynamics during SWs using spiking neurons in a recurrent network model comprised of two principal cell types. Our data provide key insights into the initiation of SWs in vivo and the activation of a recurrent network to an attractor state in silico.

Results

Two types of CA3 principal neurons. We first investigated physiological and morphological heterogeneity of pyramidal cells by obtaining whole-cell patch-clamp recordings from neurons in stratum pyramidale (SP) in acute mouse hippocampal slices (see Methods), and we assessed the intrinsic firing properties of each cell by somatic current injection. Across 103 recorded neurons, current injections at or just above action potential threshold (rheobase) yielded a bimodal distribution of initial firing frequencies (Fig. 1a,b). We refer to these as regular-spiking and bursting neurons, corresponding to low and high initial firing frequencies. Notably, however, cells that initially responded with low-frequency output could be driven at higher frequencies with sufficient current injection (Fig. 1c). The bimodality of the rheobase firing-rate distribution indicates that CA3 principal cells are divided into two functional groups; therefore, we filled a subset of neurons with biocytin to determine whether there were any morphological features that corresponded with the firing phenotypes. As expected, we found that regular-spiking neurons were decorated with complex spines (thorny excrescences), but unexpectedly, intrinsically bursting

¹Janelia Research Campus Howard Hughes Medical Institute, Ashburn, VA, USA. ²VIB Center for Brain & Disease Research, Department of Neurosciences, KU Leuven, Leuven, Belgium. ³Shenyang Institute of Automation, Chinese Academy of Sciences, Shenyang, China. *e-mail: hunt@janelia.hhmi.org; spruston@janelia.hhmi.org

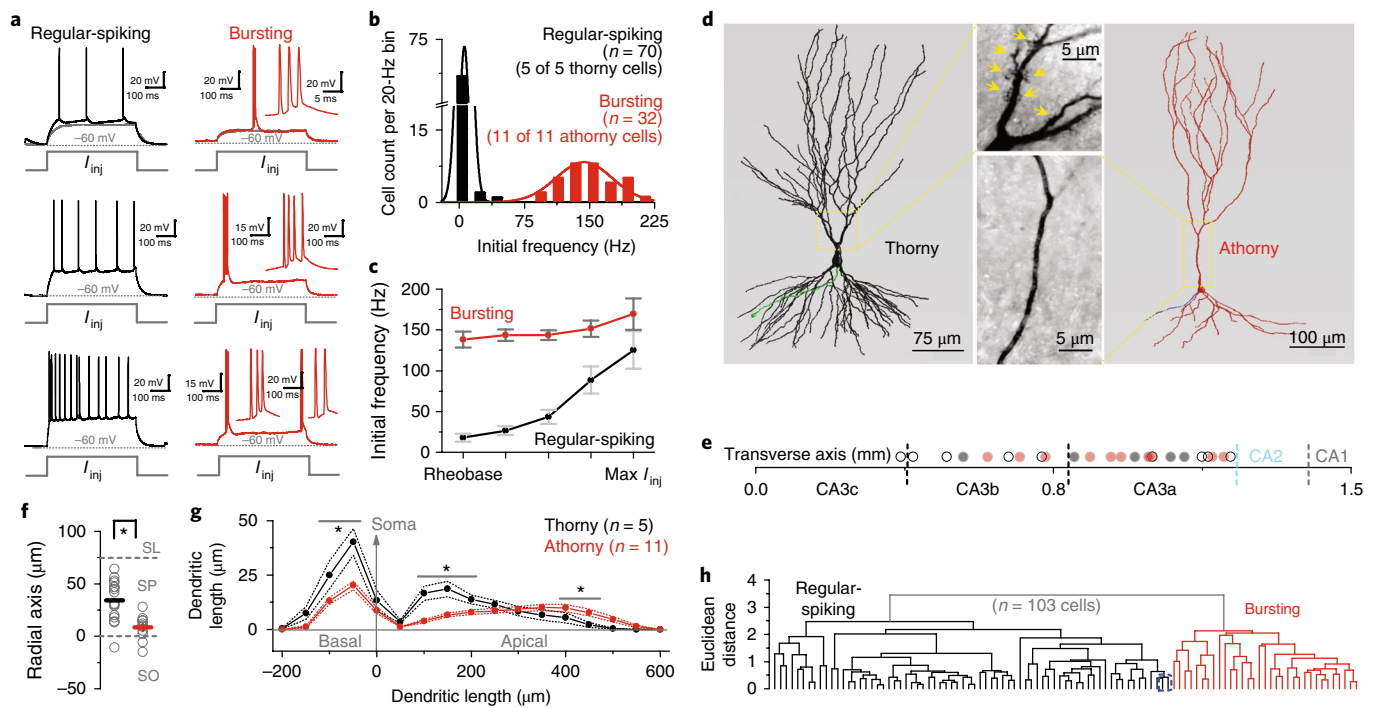


Fig. 1 | Morphofunctional phenotypes and cytoarchitecture of CA3 principal cells. **a**, Representative examples of firing patterns elicited by increasing somatic current injections (I_{inj}) for the two different physiological phenotypes of CA3 pyramidal neurons. **b**, Histogram of initial firing frequency for all CA3 pyramidal cell recordings. The bimodal structure of the histogram suggests that the CA3 principal cell population is comprised of two distinct functional phenotypes, regular-spiking and intrinsically bursting. **c**, Input-output relationship of regular-spiking and bursting neurons. For each cell, current steps are aligned to the rheobase (minimum current injection required for suprathreshold response). For regular-spiking cells, rheobase was 300 ± 25 pA and increased to maximum in 100 pA increments. For bursting cells, rheobase was 150 ± 22 pA and increased in 25 pA steps. Colored lines represent mean values for bursting (red, $n=17$) and regular-spiking (black, $n=33$) cells. Error bars for each line depict the s.e.m. **d**, Representative morphological reconstructions for (left) the regular-spiking cell shown above in **a** (dendrites, black; axon, green) and (right) the bursting neuron shown above in **a** (dendrites, red; axon, blue) following whole-cell recording in acute mouse hippocampal slices. Regular-spiking cells had thorny excrescences (left and top middle), whereas intrinsically bursting cells lacked thorns (right and bottom middle). **e**, Somatic locations along the transverse axis (bottom; 0 = beginning of pyramidal layer in proximal CA3) are indicated for full reconstructions (filled circles) and for incompletely reconstructed neurons with regular-spiking intrinsic properties (open circles). The CA2 boundary is defined by the termination of stratum lucidum (SL) and the presence of cells immunopositive for PCP4 (cyan). Here and throughout, black indicates thorny, regular-spiking cells; red indicates athorny, bursting cells. **f**, Radial axis locations for all recovered cells, segregated by intrinsic properties. Zero is defined by the border of the pyramidal layer and stratum oriens (SO); positive values indicate the direction of the apical dendrite. Note the significant difference in the mean somatic position of regular-spiking cells, indicated by the black bar ($n=16$ cells) and bursting cells, indicated by the red bar ($n=11$ cells; two-sided two-sample t test, $*P=0.00032$). **g**, Comparison of dendritic branching between thorny and athorny cells. Thorny cells have more basal and proximal apical (radial oblique) dendrites, while athorny cells have longer distal apical branches. Points with solid connecting lines depict mean dendritic length for 50- μ m spatial bins for 5 thorny cells and 11 athorny cells. Dashed lines depict the s.e.m. Significant differences between cell types were found at $-50 \mu\text{m}$ ($P=0.027$), $+50 \mu\text{m}$ ($P=0.033$), $+100 \mu\text{m}$ ($P=0.016$), $+150 \mu\text{m}$ ($P=0.024$), $+200 \mu\text{m}$ ($P=0.04$), $+450 \mu\text{m}$ ($P=0.011$), and $+500 \mu\text{m}$ ($P=0.0063$; two-sided two-sample t test). $*P < 0.05$. **h**, Dendrogram generated from hierarchical clustering of several physiological features (excluding initial firing frequency). The two clusters, indicated by color-coding of first division in the dendrogram, correspond well to the bimodal distribution of initial firing frequency, indicating that this measure is 98% accurate for cell-type characterization (2 of 103 cells were misclassified, indicated by dashed blue box).

neurons clearly lacked these structures (i.e., thorny versus athorny cells; Fig. 1d). While regular-spiking cells (5 of 5, thorny) could occupy any position along the transverse or radial axis of SP, intrinsically bursting neurons (11 of 11, athorny) were preferentially located at distal regions (CA3a and CA3b) and deeper in the pyramidal-cell layer (i.e., closer to stratum oriens; Fig. 1e,f). Moreover, we identified athorny pyramids in rats (Supplementary Fig. 1). In mice, athorny pyramidal cells were also visualized using Golgi staining or viral injection, where they were found to be negative for the vesicular GABA transporter (VGAT), a ubiquitous inhibitory marker, and positive for the glutamatergic markers VGLUT1 and VGLUT2, indicating that they are not GABAergic (Supplementary Figs. 2–4). In addition to the presence or absence of thorny excrescences and the difference in initial rheobase firing frequency, the two cell types had different dendritic morphologies (Fig. 1g and Supplementary

Fig. 5) and several distinctive physiological properties such as input resistance, action potential threshold, after-depolarizing potential, and after-hyperpolarizing potential (Supplementary Fig. 6 and Supplementary Table 1). Unsupervised clustering based on multiple physiological features supported a segregation of the CA3 pyramidal cell population into two morphological and functional phenotypes that matched the groups defined by the initial rheobase firing frequency and by the presence or absence of thorns (Fig. 1h). These data indicate that there are at least two principal cell types interspersed within the CA3 region.

Cell-type-specific mossy fiber connectivity. The conspicuous absence of thorny excrescences on deep-layer bursting cells prompted us to ask whether these pyramids receive input from the powerful ‘detonator’ synapses formed by the mossy fibers^{7,8,17}.

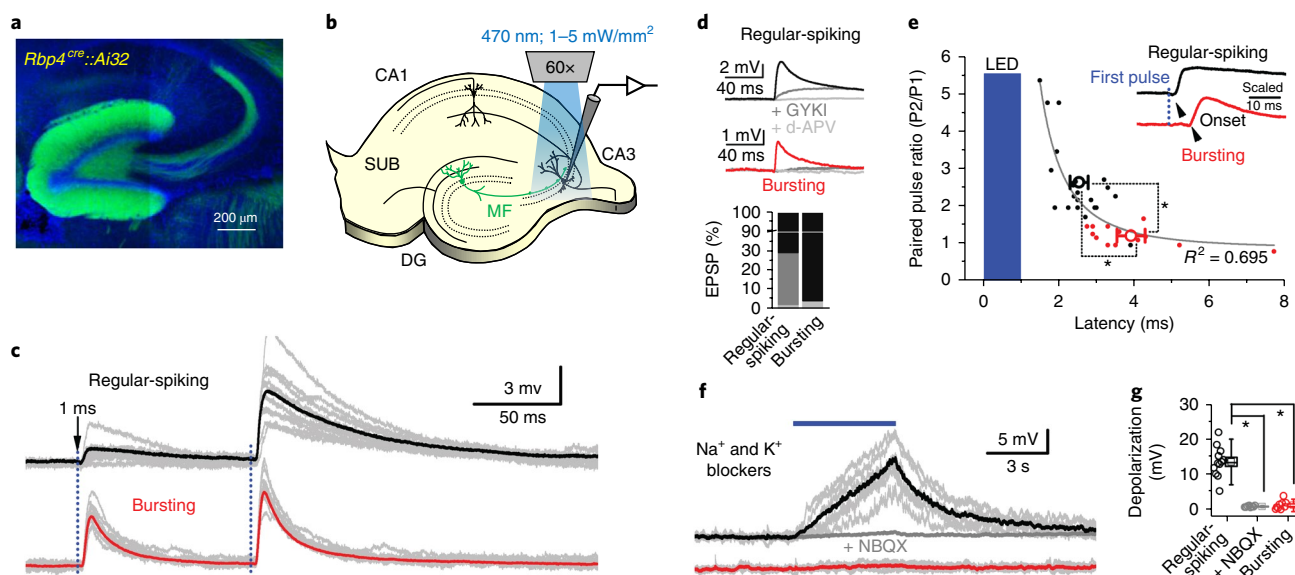


Fig. 2 | Optogenetically assisted circuit mapping of mossy-fiber synaptic connectivity. **a**, Representative expression pattern of ChR2 (green) in the dentate gyrus of *Rbp4^{cre}* mice (18 animals tested). **b**, Experimental design illustrating local full-field optical activation of mossy fibers (MF) via a 60 \times objective over a CA3 pyramidal neuron during whole-cell recording. SUB, subiculum. **c**, Representative individual traces (gray) and averages (black, red) taken from a regular-spiking cell (top, black) and a bursting cell (bottom, red) during brief optical activation (dashed blue lines) of mossy fibers. **d**, Top: representative trace averages for each cell type, indicating the control amplitude, the remaining synaptic response in the presence of the AMPA-receptor blocker GYKI (gray; 30 μ M), defining the kainate-receptor-mediated component of transmission, and the NMDA receptor (NMDAR)-mediated component, defined by the synaptic response amplitude in the presence of both GYKI and the NMDAR antagonist d-APV (50 μ M). Bottom: summary bar plot for 5 regular-spiking cells and 6 bursting cells, indicating the relative components of glutamatergic transmission of AMPAR (black), KAR (dark gray), and NMDAR-mediated transmission (light gray). **e**, Summary data for regular-spiking (black; $n=20$ cells) and bursting cells (red; $n=13$ cells) showing a correlation (parabolic fit, gray line) between the paired-pulse ratio (PPR; P_2/P_1) and the onset latency. Average values (large open circles, mean \pm s.e.m.) for both measures are significantly different between regular-spiking and bursting cells (two-sided two-sample t test, $P=0.00019$ for PPR; $P=0.00017$ for latency). Inset: expanded timescale for amplitude-normalized (scaled) responses to the first optical pulse, illustrating a delayed onset of synaptic responses for bursting cells relative to regular-spiking neurons. $*P < 0.05$. **f**, Representative individual (gray) and average traces for regular-spiking (black) and bursting (red) responses to extended optical activation (blue bar) of mossy fibers during pharmacological inactivation of recurrent activity (see Methods for details). **g**, Summary of direct mossy-fiber responses (recurrent activity blocked). Square points of box plot represent means, horizontal lines depicts medians, box limits represent s.e.m., and whiskers show s.d. We find a significant difference between regular-spiking ($n=12$) and bursting ($n=9$) cells (two-sided two-sample t test, $*P=0.0000033$). NBQX (30 μ M; $n=8$ cells) was bath applied at the end of the experiment to confirm that the response was glutamatergic (two-sided paired-sample t test, $*P=0.00016$).

To address this question, we used the *Rbp4^{cre}* transgenic mouse line, which expresses Cre-recombinase in dentate granule cells. By crossing this strain to the channelrhodopsin 2 (ChR2) reporter line (Ai32; see Methods), we attained high levels of ChR2 expression in the mossy-fiber axons of virtually all mature DG granule cells (Fig. 2a and Supplementary Fig. 7). We then performed ChR2-assisted circuit mapping (see Methods) of mossy-fiber inputs onto regular-spiking or bursting CA3 pyramidal neurons (Fig. 2b and Supplementary Fig. 7). We found that optically evoked excitatory postsynaptic potentials differed between physiological cell types, including differences in short-term plasticity (paired-pulse facilitation), latency to onset, and sensitivity to AMPA-receptor antagonism (Fig. 2c–e). Similar results were obtained using *Pomc^{cre}* mice, which have been shown to label immature granule cells^{30,31} (Supplementary Fig. 7). The relationship between the magnitude of paired-pulse facilitation and the latency to response onset (Fig. 2e) suggests that bursting cells either received weak mossy-fiber input or they could be disynaptically coupled to thorny cells via recurrent connections⁷. To distinguish between these possibilities, we pharmacologically blocked action potentials with Na⁺ and K⁺ channel blockers (see Methods), ensuring that synaptic responses were limited to direct optical activation of ChR2 in mossy fibers. After eliminating recurrent activity in this way, we were unable to detect any mossy-fiber-driven input to regular-spiking or bursting cells with

brief (1–2 ms) optical stimulation, perhaps due to the unique properties of these synapses. However, a prolonged (5 s) optical stimulation drove robust depolarization in regular-spiking cells, while no significant response was observed in bursting cells (Fig. 2f,g). Together, these results indicate that regular-spiking (thorny) cells receive monosynaptic mossy-fiber input (as expected), while intrinsically bursting (athorny) CA3 pyramidal neurons received no or undetectably little direct input from mossy fibers. Additionally, both thorny and athorny neurons received disynaptic recurrent excitation. The microcircuit architecture of bursting pyramidal neurons suggests the existence of a previously unrecognized, feedforward sublayer of athorny neurons intercalated within the CA3 recurrent network, a revision to the classical single-layer conception of CA3 circuitry⁸. In all, these data support the conjecture that morphologically and functionally unique pyramidal cells comprise distinct cell-type-specific microcircuits, raising additional questions about the functional role for these circuits in the intact brain.

Deconstructing sharp waves in vivo. To gain insight into the functional roles the two types of CA3 pyramidal neurons could play in vivo, we measured activity during SWs, which are network synchronization events known to be important for hippocampus-dependent cognitive functions^{29,32}. SWs originate from the distal CA3 and/or CA2 regions^{33–36} and are observed in a diverse range of mammalian

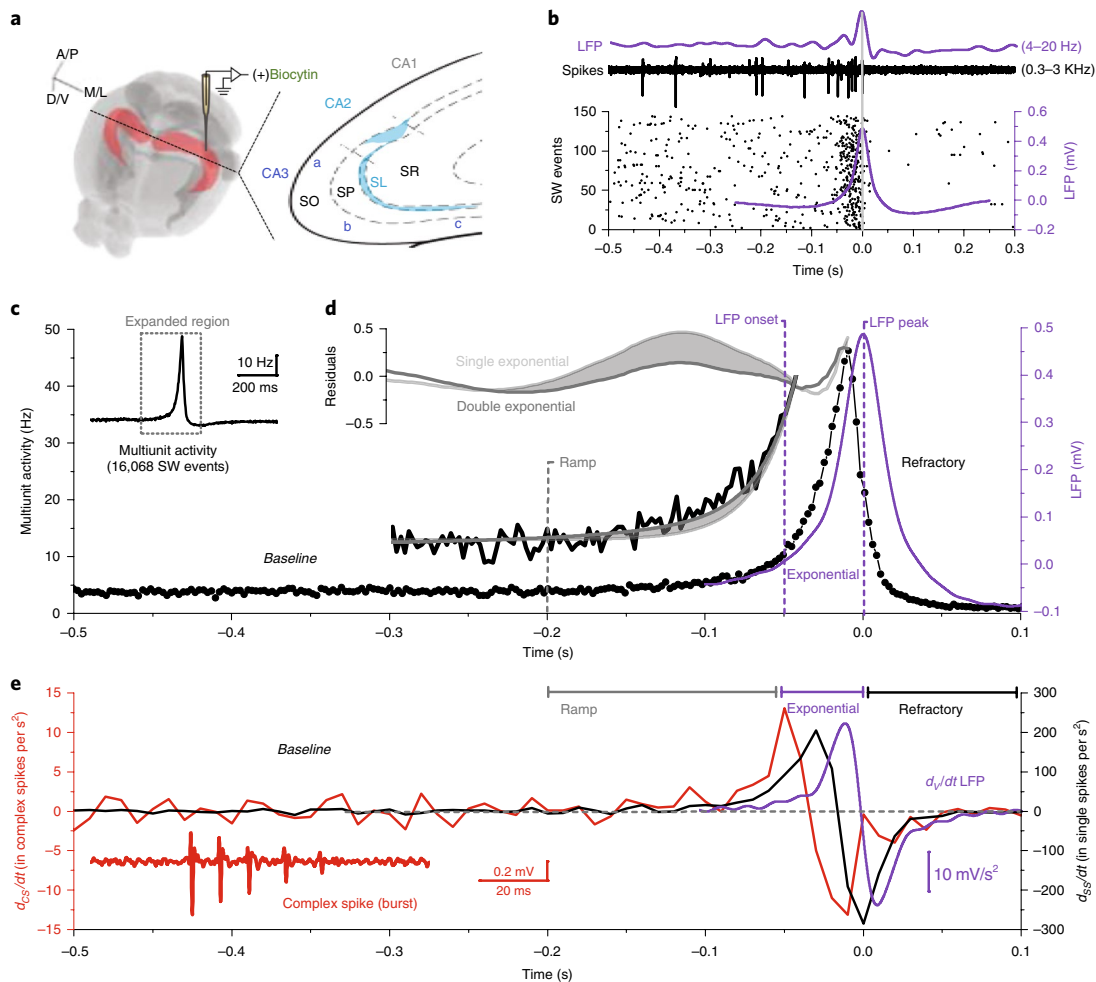


Fig. 3 | Deconstructing the spiking anatomy of sharp-wave dynamics in vivo. **a**, Schematic of experimental design for recording juxtacellular and extracellular activity in the CA3 region in vivo. A/P, anterior-posterior; M/L, medial-lateral; D/V, dorsal-ventral; SR, stratum radiatum. **b**, Top: representative traces recorded from the LFP filtered at 4–20 Hz (violet) to extract the sharp-wave LFP envelope and filtered at 0.3–3 kHz (black) to isolate action potentials. Bottom: sharp-wave LFP-triggered raster plot of MUA across 144 SW events. Vertical gray line indicates the sharp-wave peak at time = 0. Average LFP waveform (purple trace) is overlaid with spiking activity. **c**, Average SW LFP-triggered MUA across all recordings for the expanded region shown in the inset. **d**, Identification of the kinetic phases comprising a sharp wave. MUA rate during 16,068 SW events (from –300 ms to peak) was fit with a single ($\chi^2 = 0.235$, light gray line), double ($\chi^2 = 0.193$, dark gray line), or triple ($\chi^2 = 0.195$; not shown) exponential growth function, where the lowest χ^2 value was found for the double exponential function, suggesting that there are two kinetic phases in the firing-rate increase associated with the sharp-wave LFP signal. The time-course of the ramp phase is defined by the divergence in residuals between the single- and double-exponential fits (gray shaded area and violet vertical dashed lines). **e**, Sharp-wave LFP-triggered phase analysis of complex spikes extracted from sorted units (red) and single spikes (black), averaged across sorted putative units. d_{ss}/dt , first derivative of the single-spike rate; d_{cs}/dt , first derivative of the complex-spike rate. Time-courses of the different phases are indicated by labeled horizontal lines.

species from primates to rodents²⁹. These phylogenetically conserved rhythms occur spontaneously during periods of stationary wakefulness, slow-wave sleep, and under low-level anesthetics^{29,32,37}. We recorded SW-associated local field potentials (LFPs) and multiunit activity (MUA) from SP of the distal CA3 region in lightly sedated, headfixed animals (Fig. 3a,b and see Methods). Under these conditions, SWs in CA3 were associated with ripple oscillations and gave rise to both SWs and ripples in the CA1 region. Moreover, the distributions of SW interevent intervals, amplitudes, and durations under these conditions were consistent with those found in previous reports (Supplementary Fig. 8)^{29,33,34}. To understand the spiking dynamics underlying SW synchronization in greater detail, we analyzed SW LFP-triggered MUA (Fig. 3c). Aggregate MUA across all recorded SW events ($n = 16,068$) was better fit by a double exponential ($\chi^2 = 0.193$) than a single exponential ($\chi^2 = 0.235$) growth

function, suggesting two kinetic phases underlying SW generation (Fig. 3d). The time-course of the initial (ramp) phase is defined by the divergence in fit residuals, which is followed by a rapid, non-linear (exponential) increase in spiking activity. Termination of the SW is followed by a refractory period, defined by the shortest interevent interval (≈ 100 ms peak-to-peak).

Given that the primary physiological difference between the two pyramidal cell types measured *in vitro* is related to burst propensity, we sought to identify the relative contributions of complex versus single-spike activity relative to the SW. Therefore, we performed spike sorting to segregate individual cellular activity and annotated the complex spikes for each putative unit (see Methods). We then quantified the burst propensity (burst index and spikes per burst) for each putative unit (Supplementary Figs. 9 and 10). Principal component analysis (PCA) of spiking features indicated

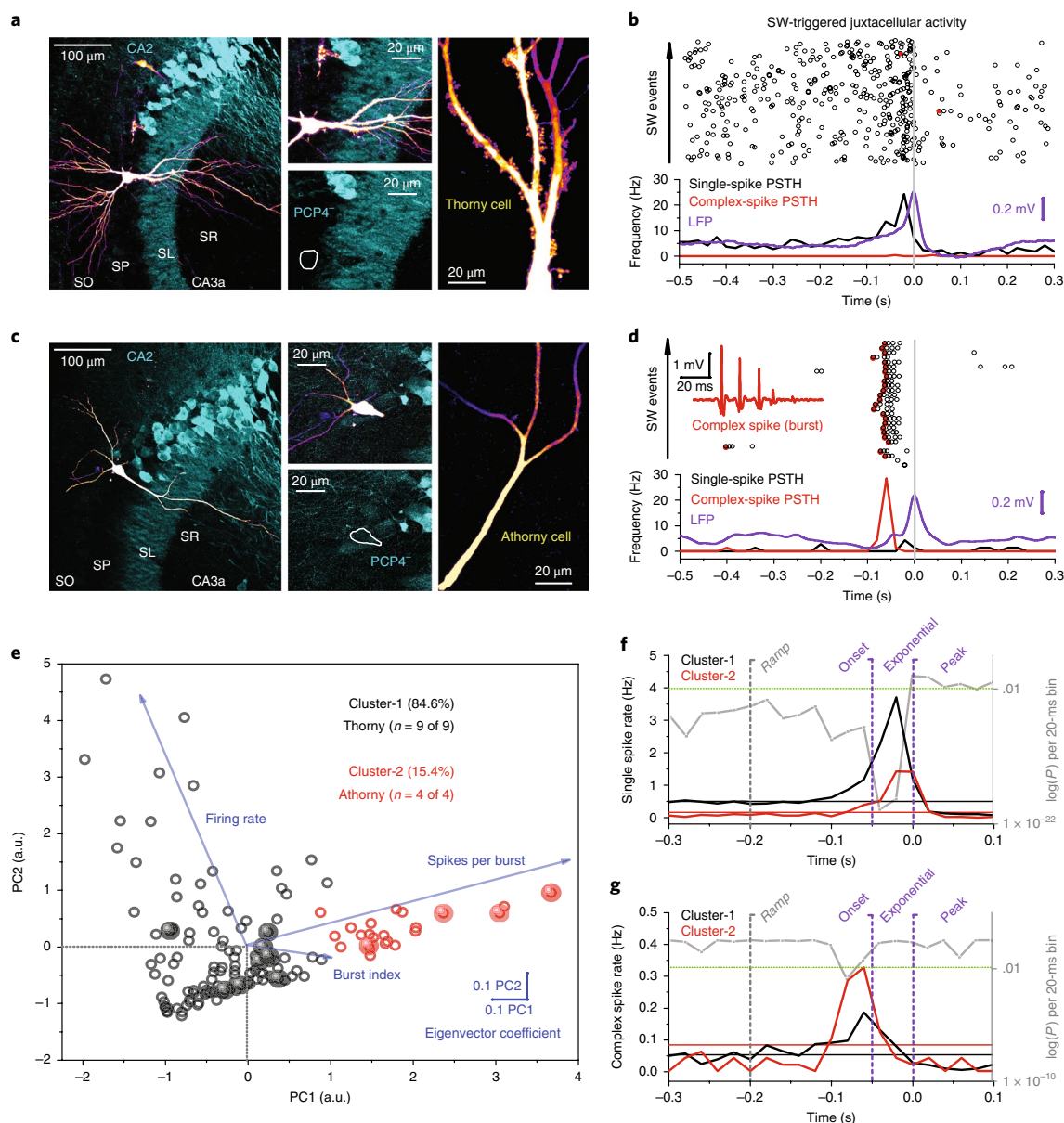


Fig. 4 | Cell-type-specific activity patterns during sharp-wave dynamics in vivo. **a**, Morphology and histology of a thorny CA3 neuron labeled following juxtacellular recordings ($n = 9$ cells). CA2 is identified by the presence of the marker PCP4 (cyan), while the recorded unit (labeled with biocytin, in pseudocolor) is PCP4⁺. The presence of thorny excrescences is clear along the proximal apical dendritic region. **b**, Single-cell summary of juxtacellular activity for the neuron labeled in **a**. Top: SW-triggered raster plot of spiking activity (black circles). Bottom: SW-triggered activity for single spikes (black) and complex spikes (red) relative to the peak of the average SW LFP waveform (violet). **c**, Morphology and histology of an athorny CA3 neuron, labeled following juxtacellular recording ($n = 4$ cells). CA2 is identified by the presence of the marker PCP4 (cyan) while the recorded unit (labeled with biocytin, in pseudocolor) is PCP4⁺. The lack of thorny excrescences is clear along the proximal apical dendritic region. **d**, Single-cell summary of juxtacellular recording for the neuron labeled in **c**. Top: SW-triggered raster plot of spiking activity (black circles). Bottom: SW-triggered activity for single spikes (black) and complex spikes (red) relative to the peak of the average SW LFP waveform (violet). Note the very few complex spikes emitted by the thorny cell while the athorny cell exhibits consistent complex spiking before SW onset. **e**, PCA of cellular firing properties for all juxtacellular units ($n = 142$). Eigenvectors (superimposed, blue) are shown for the cellular features used in PCA, plotted relative to the first two principal components. Nearest-neighbor clustering of juxtacellular units, based on PCA, identifies two principal clusters. The primary cluster (cluster-1) encompassed all nine juxtacellularly labeled thorny cells (black spheres); the secondary cluster (cluster-2) contained the four recovered athorny cells (red spheres). **f**, Population analysis of cell-type-specific activity patterns during SWs. SW-triggered single-spike perstimulus time histogram (PSTH) for cluster-1 (black, $n = 117$ cells) and cluster-2 (red, $n = 23$ cells). Correspondingly colored horizontal lines indicate the upper bound of a 99% confidence interval (based on shuffling spike times 1,000 \times), indicating significant phase-locking of activity. Statistical significance between cluster-1 and cluster-2 PSTHs is plotted on the right vertical axis (gray), where the horizontal green line indicates $P = 0.01$ (see Methods). **g**, As in **f** but for SW-triggered complex spikes.

that firing rate and burst propensity were orthogonal properties. However, a cluster analysis did not reveal any clear segregation among these extracellularly recorded units. To understand the

relationship of complex- versus single-spike activity relative to the SW, we constructed SW-triggered complex- and single-spike rate averages for SW events with greater than 0.3 s interevent intervals

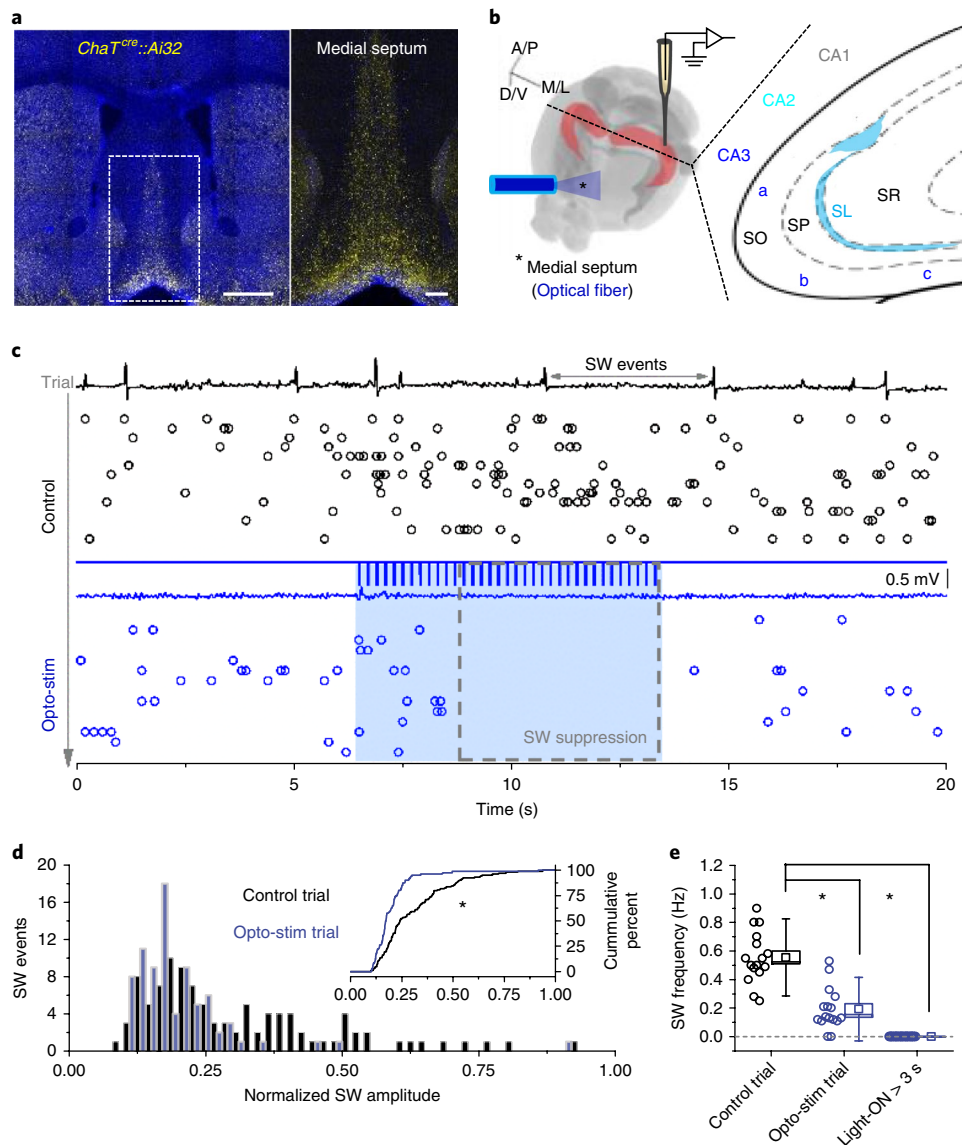


Fig. 5 | Cholinergic neuromodulation of sharp waves in vivo. **a**, Left, representative expression of ChR2 (yellow) in the *Chat^{Cre}::Ai32* mouse ($n = 6$ animals tested); scale bar, 500 μm . Right: expanded view of the inset region (white box) shown in the left panel. Scale bar, 150 μm . Note robust expression of ChR2 in the medial septal region. **b**, Schematic of experimental design for in vivo recording of SW activity in the CA3 regions a, b, and c, as well as optogenetic activation of cholinergic neurons in the medial septum. **c**, Raster plot of SW events (open circles), with representative trace shown on top, during control trial conditions (black) and during optical activation of cholinergic cells in the medial septum ('opto-stim' trials, blue shading, 8 s of 100-ms pulsed light at 5 Hz). Grey dashed box indicates the period of SW suppression quantified below. **d**, Histogram of SW-event amplitudes during control trial (black, 103 events) and opto-stim trials (blue, 80 events). Inset: cumulative percentage of SW amplitude is significantly different between control and opto-stim conditions (two-sided two-sample Kolmogorov-Smirnov (KS) test, $*P = 0.000065$). **e**, Summary of SW suppression following optical stimulation. The frequency of SW events was quantified for each trial in control trials (black $n = 16$ trials), opto-stim trials (blue $n = 16$ trials), and epochs with light-ON > 3 s (indicated by the grey dashed box in **c**). Optical stimulation of cholinergic cells significantly reduced the frequency of SW events between control trial and opto-stim trial conditions (two-sided paired-sample t test, $*P = 0.000037$), and between control and light-ON conditions (two-sided paired-sample t test, $*P = 3.1 \times 10^{-9}$).

and performed a phase analysis to delineate the sequence of events underlying network synchronization (Fig. 3e). Both complex and single-spike rates begin to increase during the ramp phase, perhaps arising due to spontaneous fluctuations in the baseline activity. The increase in complex spiking peaked at the transition from the ramp phase to the exponential phase, whereas the increase in single spiking peaked in the middle of the exponential phase. Additionally, we found that the LFP followed the dynamics of single-spike activity with short temporal latency, indicating that the LFP signature of the SW was generated by synchronization of multiple cells emitting just

a few single spikes (i.e., not bursting). Together, these data suggest an important role for complex spiking in promoting the transition from the ramp to an exponential increase in single-spike activity generating the SW LFP. However, without knowing the morphological identity (i.e., thorny vs. athorny) of the recorded units, the cell-type-specific contributions to the different phases of the SW remain uncertain.

Cell-type-specific activity during sharp waves. To determine whether thorny and athorny cells play different roles during SW

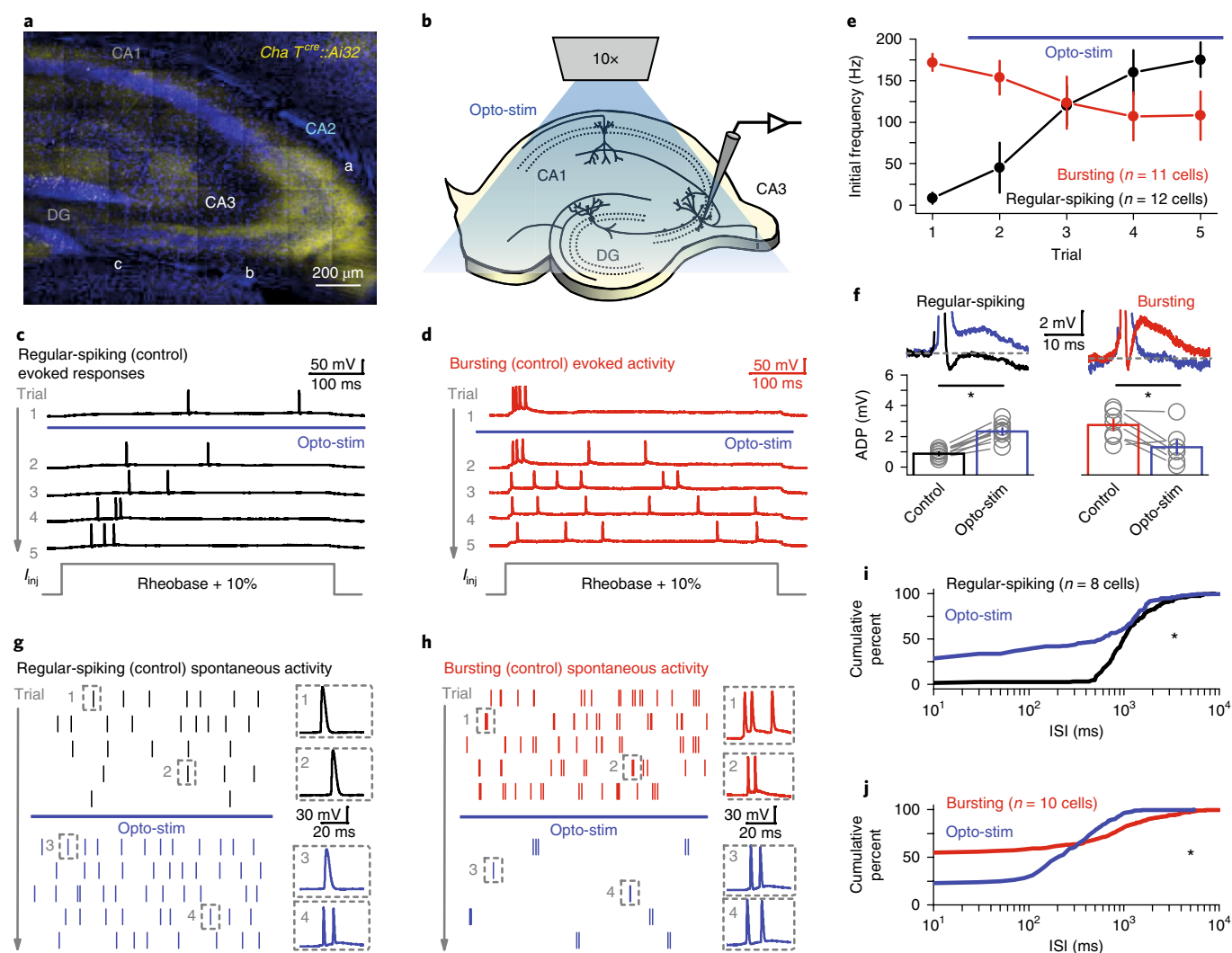


Fig. 6 | Cholinergic countermodulation of cellular intrinsic properties in vitro. **a**, Representative histological section from a *Chat^{cre}::Ai32* animal, illustrating robust ChR2 expression (yellow) in the CA3 region of the hippocampus (13 animals tested). The image was acquired in a tiled manner at 63× magnification to visualize the thin cholinergic fibers. **b**, Schematic of experimental design for full-field optical activation of cholinergic fibers (opto-stim, 10-s, 5-Hz pulse train) using a 10× objective during whole-cell recording from CA3 pyramidal neurons. **c**, Representative traces from a regular-spiking neuron. Several trains of opto-stim increased the initial firing frequency. **d**, Similar data for an intrinsically bursting cell. Repeated opto-stim reduced the initial firing frequency. **e**, Summary data averaged across cells (mean ± s.e.m.) demonstrating the countermodulation of initial firing frequency in the two cell types. **f**, Countermodulation in burst propensity corresponds with a significant counterregulation of the after-depolarizing potential (ADP; two-sided paired-sample *t* test, **P* = 0.000062, *n* = 8 regular spiking cells; **P* = 0.02, *n* = 7 bursting cells). Note that modulations of the ADP are in opposite directions for regular-spiking cells relative to bursting cells. **g**, Raster plot demonstrating the effect of opto-stim on spontaneous spiking activity in a regular-spiking cell. Opto-stim increased the firing frequency and burst propensity. Numbered insets (right) correspond to traces from the numbered boxed regions in the raster. **h**, Similar data for an intrinsically bursting cell. Opto-stim decreased firing frequency and burst propensity. **i**, Summary data indicating that interspike intervals in control trials (black, *n* = 6 cells) and during opto-stim (blue) are significantly different for regular spiking cells (two-sided two-sample KS test, **P* = 3.1 × 10⁻⁷). **j**, Summary data demonstrating that interspike intervals in control (red, *n* = 7 cells) and during opto-stim (blue) are significantly different for bursting cells (two-sided two-sample KS test, **P* = 4.5 × 10⁻⁸). Note that modulations of the interstimulus interval distribution are in opposite directions for regular-spiking relative to bursting cells.

synchronization events in vivo, we performed juxtacellular recordings to obtain high-resolution single-unit activity, in conjunction with MUA and LFP signals. Additionally, we successfully labeled a subset of cells with biocytin, allowing us to unambiguously correlate morphological and physiological phenotypes in vivo (Fig. 4a–d and Supplementary Fig. 11). For all recorded units, we extracted the single-unit features of firing rate, burst index, and spikes per burst, as before (Supplementary Fig. 10). We then employed a dimensionality-reduction strategy of PCA followed by cluster assignment based on local observation density and the distance between density peaks

in two-dimensional PCA space (Fig. 4e and see Methods). This strategy yielded two clusters, which confirmed that thorny cells had 100% correspondence to cluster-1 and that athorny cells had 100% correspondence to cluster-2. Using these cluster designations to analyze cell-type-specific activity during SWs across cells, we constructed SW-triggered averages for single-spike and complex-spike activity for all units within each cluster (Fig. 4f,g). Cluster-1 (thorny) cells predominantly contributed single spikes to baseline activity, increased their single-spike rate during the ramp phase, and peaked single-spike activity during the exponential phase. In contrast,

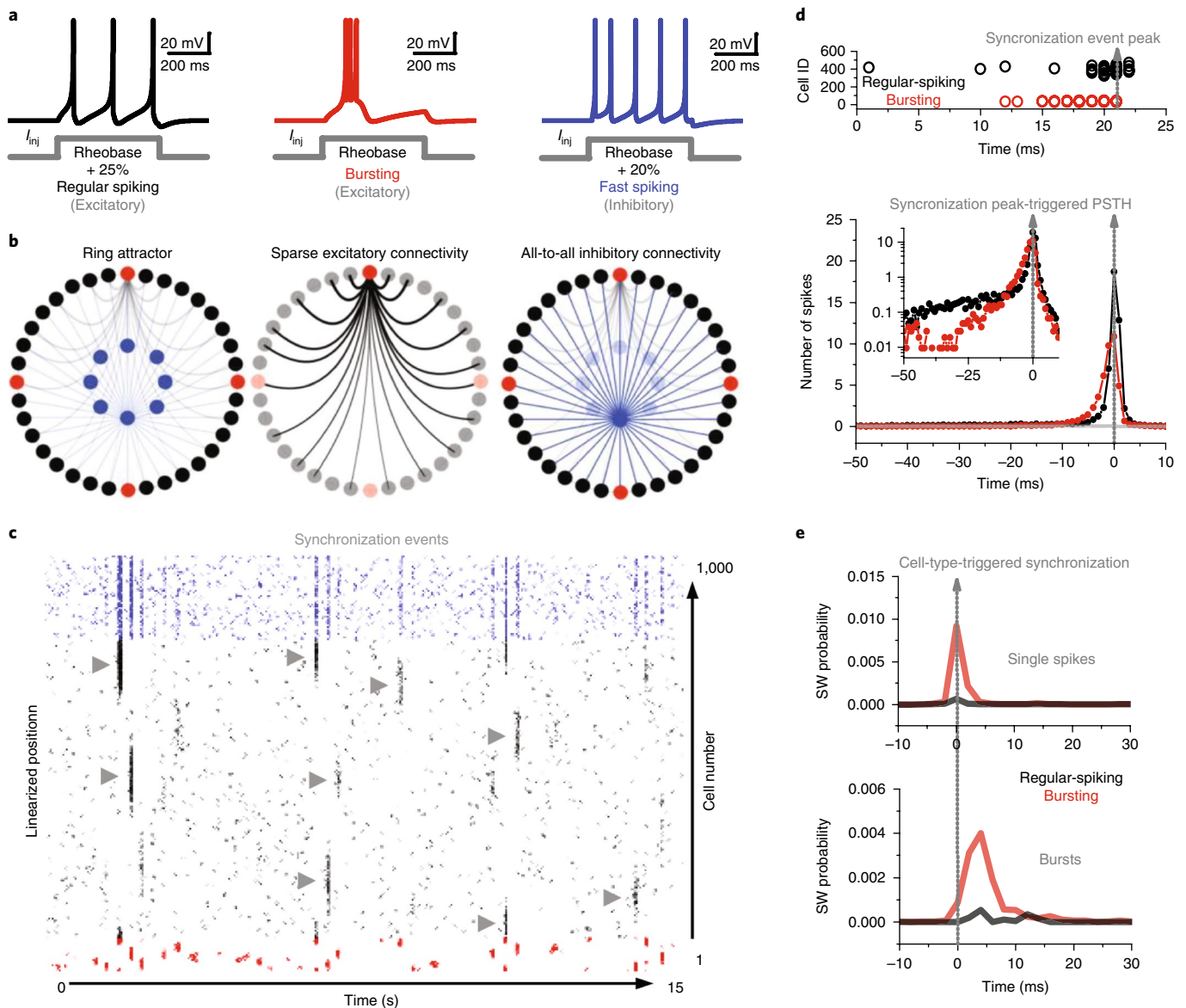


Fig. 7 | Cell-type-specific roles during synchronization dynamics in silico. **a**, Intrinsic properties of the cell types incorporated into the network model. Two different excitatory cell types were tuned to have regular-spiking (black) and intrinsically bursting (red) firing patterns, analogous to thorny and athorny cells, respectively. A single fast-spiking inhibitory cell type was also included (blue). **b**, Ring-attractor network architecture comprised of the cell types in **a**. The network features sparse distance-dependent excitatory connectivity and all-to-all inhibitory connectivity. **c**, Raster plot of network activity tuned to exhibit partial synchronization for a given cell type's composition and synaptic weight distribution during 15 s of simulation time. Vertical bands, synchronization events (gray arrowheads). **d**, Top: single synchronization event isolated from the network depicting the regular-spiking (black) and bursting (red) cells participating in the ensemble synchronization. Note the bursting cell activity preceding the synchronization peak (gray vertical arrow). Bottom: synchronization-peak-triggered PSTH for regular-spiking (black) and bursting cells (red) activity plotted on a linear scale. Inset: same data plotted on a logarithmic scale so that the slow 'ramp-like' component of the regular-spiking cells can be seen. Note that the bursting cell activity increases before the peak rate increase (indicated by vertical dashed arrow) observed in the regular-spiking cells. **e**, Spike-triggered synchronization probability for regular-spiking (black) and bursting cells (red). Top: vSW probability triggered by single-spike events peaks at time zero (during the synchronization event). Bottom: SW probability triggered by burst events. Note peak and positive offset of bursts emitted by bursting cells (red), indicating the relatively high probability that bursting cell firing occurs within a SW and that their burst firing occurs at the onset of SWs.

cluster-2 (athorny) cells contributed very little to background activity and relatively weakly increased their single-spike rate during the ramp and exponential phases of the SW. Both cluster-1 (thorny) and cluster-2 (athorny) units increased their complex-spike rate late in the ramp phase, before the onset of exponential phase. Notably, this increase in complex-spike rate was significantly greater for cluster-2 (athorny) cells. Additionally, cluster-1 and cluster-2 exhibited differential phase-specific participation during SWs (Supplementary Fig. 12 and see Methods). Together, these results demonstrate a dynamic

interplay between the constituent units of the CA3 network, indicating that athorny cells contribute to SWs predominantly through burst firing during the ramp phase and thorny cells contribute predominantly single-spike activity during the ramp and exponential phases, largely generating the LFP signature of the SW.

Neuromodulation of sharp waves and cellular properties. Hippocampal network states are known to be under the control of cholinergic neuromodulation, which is thought to regulate

opposing aspects of cognitive function^{29,38}. To explore how neuromodulation effects SW generation by CA3 in vivo, we recorded SW activity in CA3 while optogenetically activating the cholinergic cells of the medial septum of mice expressing ChR2 under the choline acetyltransferase promoter (*ChaT^{Cre}::Ai32*; Fig. 5a–c). Under control conditions, we observed aperiodic SW events as described above. However, optical activation of cholinergic neurons completely abolished SWs after a few seconds of light delivery. In addition, a residual inhibition of the amplitude and frequency of SWs was observed in seconds-long periods in between light-delivery epochs (Fig. 5d–f). These data indicate that, at the purported site of generation (i.e., the CA3 region), SW synchronization is regulated by cholinergic neuromodulation, consistent with previous reports from the CA1 region^{39,40}.

To discern how cell-type-specific activity is modulated by cholinergic input to produce the overall SW desynchronizing effect we observed in vivo, we mimicked the transition between brain states in vitro by optically activating cholinergic fibers innervating hippocampal slices (Fig. 6a,b). Trains of full-field pulsed illumination (see Methods) during whole-cell recording increased the initial firing frequency of regular-spiking cells, driven by somatic current injections of the same amplitude. Conversely, cholinergic activation decreased the initial frequency of bursting neurons. This countermodulation of burst propensity likely resulted primarily from reciprocal modulation of the after-depolarizing potential (Fig. 6c–f). Cholinergic countermodulation of burst propensity was also observed in the spontaneous firing of these cells, which was presumably driven by spontaneous synaptic activity in the recurrent network (Fig. 6g–j). Additionally, we confirmed that cholinergic countermodulation was also a feature of regular-spiking and bursting pyramidal cells of the rat hippocampus (Supplementary Fig. 1). Together, these data demonstrate a relationship between cholinergic modulation of the synchronization state of the CA3 recurrent network and countermodulation of cell-type-specific intrinsic properties. The prominent downregulation of athorny cell burst propensity by acetylcholine suggests that their ability to promote SWs is disabled when mossy-fiber input to a cellular ensemble defines the attractor state of the network, facilitating pattern separation and memory encoding. In a low-cholinergic state, however, athorny cell bursting facilitates reactivation (i.e., replay) of attractor states in the form of SWs.

Synchronization of an attractor network in silico. To gain insight into how cell-type-specific firing patterns arise during network synchronization dynamics, we constructed a ring attractor recurrent network model comprised of two populations of excitatory cell types tuned to have regular-spiking or bursting properties, as well as a population of fast-spiking inhibitory cells (Fig. 7a and Supplementary Fig. 13). Other structural features of the model include distance-dependent sparse recurrent connectivity among excitatory cell types, where nearest-neighbor connections are most abundant and decay with distance along the ring, and all-to-all inhibitory connectivity (Fig. 7b). Excitatory-to-excitatory synapses were endowed with short-term synaptic plasticity (see Methods). When driven by stochastic input delivered to regular-spiking and inhibitory units, our network produces SW-like synchronized events (i.e., aperiodic epochs of partial network synchronization, which we refer to as virtual sharp waves (vSWs; Fig. 7c). We next explored the synchronization state-space of our model by varying the proportion of bursting cells in the network by the synaptic strength to understand how these parameters influenced vSW dynamics. We found that increasing recurrent synaptic weight or incorporating a larger fraction of bursting units both promote the occurrence of vSWs. However, the inclusion of bursting units facilitates the occurrence of vSWs at lower values of synaptic strength relative to a network comprised of regular-spiking units alone. Moreover, a sparse population

of bursting units (10% in our simulations) reduces the percentage of regular-spiking units recruited into a given vSW across a range of synaptic weights (Supplementary Fig. 14).

To compare how the spiking dynamics in the model relate to those measured in vivo, we constructed vSW-triggered averages for regular-spiking and bursting cells (Fig. 7d). We found that the cell-type-specific firing patterns in our network model recapitulate the cell-type-specific dynamics measured in vivo: namely, bursting-unit activity preceded population synchrony and the expression of an attractor state. Furthermore, we analyzed the probability of each cell type in our model to drive network synchronization and found that activity of bursting neurons has the highest probability of evoking vSWs (Fig. 7e). Taken together, our simulations highlight a unique role for bursting (athorny) cells in promoting SW synchronization.

Discussion

Using diverse experimental approaches, our study reveals the presence of a previously unrecognized pyramidal cell type in the CA3 region. These neurons occupy a distinct cytoarchitectural position (deep-layer SP in CA3a and CA3b), and they have unique morphological attributes (most notably their lack of thorns) and functional properties (bursting). Previous studies likely overlooked this cell type because athorny neurons constitute a minority of pyramids (~10–20%). Moreover, mossy-fiber input from DG (10⁶ cells) converge onto CA3 (3 × 10⁵ cells) with sparse connectivity (~40 thorns per cell, each of which receives input from a single mossy fiber). The sparse convergence of DG-to-CA3 circuitry—convolved with the additional confound of polysynaptic contamination⁷—make it prohibitively difficult to distinguish between cells with and without direct mossy-fiber inputs using conventional approaches. We overcame this obstacle by using an optogenetic approach to disambiguate mossy-fiber responses from recurrent synaptic responses, revealing that athorny cells receive very little or no mossy-fiber input.

Mounting evidence indicates that across the hippocampal transverse axis, heterogeneity exists within the principal cell populations previously considered to be monolithic^{27,28}. Moreover, this heterogeneity has cytoarchitectural organization, indicated by laminar segregation of cell-type-specific microcircuitry^{22,25,26,36}. The discovery of athorny neurons and their unique integration in the microcircuit suggests a revision to the classical single-layer concept of CA3, to include an interdigitated feedforward sublayer and prompting our investigation into the function of this sublayer in the intact brain. In vivo, CA3 generates SWs, the disruption of which causes memory deficits^{41–44}, thus demonstrating their cognitive salience. We posit a cellular mechanism for SW generation by dissecting the cell-type-specific spiking anatomy of SW synchronization in vivo, establishing a key role for athorny cell bursts as triggers of SWs.

The occurrence of SWs is brain-state-dependent, where cholinergic tone is thought to arbitrate between different degrees of network synchronization^{29,32,38}. We corroborated that increasing cholinergic tone leads to SW desynchronization in vivo by optogenetically eliciting acetylcholine release^{39,40}. In vitro, this manipulation reveals that countermodulation of the intrinsic excitability of CA3 cell types contributes to cholinergic regulation of SW synchronization. A parsimonious interpretation of these findings suggests that by reducing athorny cell excitability, high-cholinergic tone enables separated input patterns relayed by mossy fibers to drive thorny-cell ensembles into a unique attractor basin. Coincident firing of mossy-fiber-triggered CA3 ensembles then modifies recurrent synaptic weights during auto-associative memory encoding^{14,18}. When acetylcholine levels decrease, excitability of thorny cells is reduced such that they fire just a few (1–3) single spikes during SWs. Conversely, burst propensity of athorny neurons increases, permitting the emergence of SWs promoted by athorny cell bursting.

In many cases the relationship between neural circuit activity and the computations implemented by their dynamics is unclear. However, establishing this relationship is of paramount importance for demystifying the neural underpinnings of cognition. It has been suggested that SW attractor states reflect pattern completion computations vital to memory function. Evidence in support of this relationship comes from the observation that cellular activity patterns occurring during recent experiences are reactivated in temporally compressed synchronous epochs (SW replay). In the context of our findings, information about cell assembly patterns stored at recurrent synapses can be reactivated during SWs when driven by internally generated and/or extrinsic partial patterns, where readout of these partial patterns is performed by athorny cells⁴⁵, promoting pattern completion manifested as a SW attractor.

We provide insight into the relationship between SW attractor dynamics and pattern completion using a data-driven artificial neural network. By tuning single-cell and network parameters to recapitulate the cell-type-specific activity measured *in vitro* and during SWs *in vivo*, synchronization events *in silico* have explanatory power for understanding the neural correlates of pattern completion. *In silico*, aperiodic synchronization emerges from the asynchronous state when stochastic correlations are amplified from the baseline activity of regular-spiking (thorny) units. These spontaneous correlations arise from the structure of synaptic weights among neurons and therefore represent partial ensemble patterns. Full-ensemble reactivation (i.e., pattern completion) is facilitated when bursting (athorny) units emit complex spikes in response to correlated input, providing the essential nonlinearity around which thorny neuron single spikes can synchronize. This dynamic interplay between CA3 cell types delineates how synaptically stored memory can be extracted to spiking form, manifested as ensemble synchronization or an attractor state.

An appropriate analogy for the functional role of the athorny sublayer is the hidden layer of artificial recurrent neural networks, such as the Boltzmann machine⁴⁶. The utility of this comparison is evident, in that relevant correlational structures present in the stochastic activity of the visible layer (thorny cell layer in CA3) are processed nonlinearly (amplified via bursting) by the hidden layer (athorny sublayer) and transmitted back to the visible layer. Moreover, bursting provides a powerful means of information transfer in recurrent networks^{35,47–49}, enabling the selective routing of information among cellular ensembles⁵⁰. Specifically, the incipient property athorny cell bursting imparts on the CA3 recurrent network suggests that the moniker ‘inceptor cells’ would be particularly apt, as they induce SW synchronization, re-instantiating previously stored representations. While we provide the first evidence of this cell type and uncover a vital functional role for them, future studies will be necessary to discern their full repertoire of functionality in physiological and pathological brain states.

Methods

Methods, including statements of data availability and any associated accession codes and references, are available at <https://doi.org/10.1038/s41593-018-0172-7>.

Received: 21 August 2017; Accepted: 26 April 2018;
Published online: 18 June 2018

References

- Guzman, S. J., Schlögl, A., Frotscher, M. & Jonas, P. Synaptic mechanisms of pattern completion in the hippocampal CA3 network. *Science* **353**, 1117–1123 (2016).
- Knierim, J. J. & Neunuebel, J. P. Tracking the flow of hippocampal computation: pattern separation, pattern completion, and attractor dynamics. *Neurobiol. Learn. Mem.* **129**, 38–49 (2016).
- Leutgeb, J. K., Leutgeb, S., Moser, M. B. & Moser, E. I. Pattern separation in the dentate gyrus and CA3 of the hippocampus. *Science* **315**, 961–966 (2007).
- McHugh, T. J. et al. Dentate gyrus NMDA receptors mediate rapid pattern separation in the hippocampal network. *Science* **317**, 94–99 (2007).
- Neunuebel, J. P. & Knierim, J. J. CA3 retrieves coherent representations from degraded input: direct evidence for CA3 pattern completion and dentate gyrus pattern separation. *Neuron* **81**, 416–427 (2014).
- Rolls, E. T. The mechanisms for pattern completion and pattern separation in the hippocampus. *Front. Syst. Neurosci.* **7**, 74 (2013).
- Henze, D. A., Urban, N. N. & Barrionuevo, G. The multifarious hippocampal mossy fiber pathway: a review. *Neuroscience* **98**, 407–427 (2000).
- Rebola, N., Carta, M. & Mulle, C. Operation and plasticity of hippocampal CA3 circuits: implications for memory encoding. *Nat. Rev. Neurosci.* **18**, 208–220 (2017).
- Knierim, J. J. & Zhang, K. Attractor dynamics of spatially correlated neural activity in the limbic system. *Annu. Rev. Neurosci.* **35**, 267–285 (2012).
- Colgin, L. L. et al. Attractor-map versus autoassociation based attractor dynamics in the hippocampal network. *J. Neurophysiol.* **104**, 35–50 (2010).
- Rennó-Costa, C., Lisman, J. E. & Verschure, P. F. A signature of attractor dynamics in the CA3 region of the hippocampus. *PLoS Comput. Biol.* **10**, e1003641 (2014).
- Hopfield, J. J. Neural networks and physical systems with emergent collective computational abilities. *Proc. Natl Acad. Sci. USA* **79**, 2554–2558 (1982).
- Marr, D. Simple memory: a theory for archicortex. *Phil. Trans. R. Soc. Lond. B* **262**, 23–81 (1971).
- Mcnaughton, B. L. & Morris, R. G. M. Hippocampal synaptic enhancement and information-storage within a distributed memory system. *Trends Neurosci.* **10**, 408–415 (1987).
- Treves, A. & Rolls, E. T. Computational analysis of the role of the hippocampus in memory. *Hippocampus* **4**, 374–391 (1994).
- No, R. Ld Studies on the structure of the cerebral cortex. II, Continuation of the study of the ammonic system. *J. Psychol. Neurol.* **46**, 113–177 (1934).
- Henze, D. A., Wittner, L. & Buzsáki, G. Single granule cells reliably discharge targets in the hippocampal CA3 network *in vivo*. *Nat. Neurosci.* **5**, 790–795 (2002).
- Hunt, D. L., Puente, N., Grandes, P. & Castillo, P. E. Bidirectional NMDA receptor plasticity controls CA3 output and heterosynaptic metaplasticity. *Nat. Neurosci.* **16**, 1049–1059 (2013).
- Lee, H., Wang, C., Deshmukh, S. S. & Knierim, J. J. Neural population evidence of functional heterogeneity along the CA3 transverse axis: pattern completion versus pattern separation. *Neuron* **87**, 1093–1105 (2015).
- Lu, L., Igarashi, K. M., Witter, M. P., Moser, E. I. & Moser, M. B. Topography of place maps along the CA3-to-CA2 axis of the hippocampus. *Neuron* **87**, 1078–1092 (2015).
- Bilkey, D. K. & Schwartzkroin, P. A. Variation in electrophysiology and morphology of hippocampal CA3 pyramidal cells. *Brain Res.* **514**, 77–83 (1990).
- Marissal, T. et al. Pioneer glutamatergic cells develop into a morpho-functionally distinct population in the juvenile CA3 hippocampus. *Nat. Commun.* **3**, 1316 (2012).
- Hemond, P. et al. Distinct classes of pyramidal cells exhibit mutually exclusive firing patterns in hippocampal area CA3b. *Hippocampus* **18**, 411–424 (2008).
- Witter, M. P. Intrinsic and extrinsic wiring of CA3: indications for connectional heterogeneity. *Learn. Mem.* **14**, 705–713 (2007).
- Kohara, K. et al. Cell type-specific genetic and optogenetic tools reveal hippocampal CA2 circuits. *Nat. Neurosci.* **17**, 269–279 (2014).
- Danielson, N. B. et al. Sublayer-specific coding dynamics during spatial navigation and learning in hippocampal area CA1. *Neuron* **91**, 652–665 (2016).
- Graves, A. R. et al. Hippocampal pyramidal neurons comprise two distinct cell types that are countermodulated by metabotropic receptors. *Neuron* **76**, 776–789 (2012).
- Lee, S. H. et al. Parvalbumin-positive basket cells differentiate among hippocampal pyramidal cells. *Neuron* **82**, 1129–1144 (2014).
- Buzsáki, G. Hippocampal sharp wave-ripple: a cognitive biomarker for episodic memory and planning. *Hippocampus* **25**, 1073–1188 (2015).
- Overstreet, L. S. et al. A transgenic marker for newly born granule cells in dentate gyrus. *J. Neurosci.* **24**, 3251–3259 (2004).
- Nakashiba, T. et al. Young dentate granule cells mediate pattern separation, whereas old granule cells facilitate pattern completion. *Cell* **149**, 188–201 (2012).
- Carr, M. F., Jadhav, S. P. & Frank, L. M. Hippocampal replay in the awake state: a potential substrate for memory consolidation and retrieval. *Nat. Neurosci.* **14**, 147–153 (2011).
- Csicsvari, J., Hirase, H., Mamiya, A. & Buzsáki, G. Ensemble patterns of hippocampal CA3-CA1 neurons during sharp wave-associated population events. *Neuron* **28**, 585–594 (2000).
- Wittner, L. & Miles, R. Factors defining a pacemaker region for synchrony in the hippocampus. *J. Physiol. (Lond.)* **584**, 867–883 (2007).
- Miles, R. & Wong, R. K. Single neurones can initiate synchronized population discharge in the hippocampus. *Nature* **306**, 371–373 (1983).

36. Oliva, A., Fernández-Ruiz, A., Buzsáki, G. & Berényi, A. Role of hippocampal CA2 region in triggering sharp-wave ripples. *Neuron* **91**, 1342–1355 (2016).
37. Lustig, B., Wang, Y. & Pastalkova, E. Oscillatory patterns in hippocampus under light and deep isoflurane anesthesia closely mirror prominent brain states in awake animals. *Hippocampus* **26**, 102–109 (2016).
38. Hasselmo, M. E. The role of acetylcholine in learning and memory. *Curr. Opin. Neurobiol.* **16**, 710–715 (2006).
39. Norimoto, H., Mizunuma, M., Ishikawa, D., Matsuki, N. & Ikegaya, Y. Muscarinic receptor activation disrupts hippocampal sharp wave-ripples. *Brain Res.* **1461**, 1–9 (2012).
40. Vandecasteele, M. et al. Optogenetic activation of septal cholinergic neurons suppresses sharp wave ripples and enhances theta oscillations in the hippocampus. *Proc. Natl Acad. Sci. USA* **111**, 13535–13540 (2014).
41. Girardeau, G., Benchenane, K., Wiener, S. I., Buzsáki, G. & Zugaro, M. B. Selective suppression of hippocampal ripples impairs spatial memory. *Nat. Neurosci.* **12**, 1222–1223 (2009).
42. Jadhav, S. P., Kemere, C., German, P. W. & Frank, L. M. Awake hippocampal sharp-wave ripples support spatial memory. *Science* **336**, 1454–1458 (2012).
43. Nakashiba, T., Young, J. Z., McHugh, T. J., Buhl, D. L. & Tonegawa, S. Transgenic inhibition of synaptic transmission reveals role of CA3 output in hippocampal learning. *Science* **319**, 1260–1264 (2008).
44. van de Ven, G. M., Trouche, S., McNamara, C. G., Allen, K. & Dupret, D. Hippocampal offline reactivation consolidates recently formed cell assembly patterns during sharp wave-ripples. *Neuron* **92**, 968–974 (2016).
45. Buzsáki, G. Neural syntax: cell assemblies, synapsembles, and readers. *Neuron* **68**, 362–385 (2010).
46. Ackley, D. H., Hinton, G. E. & Sejnowski, T. J. A learning algorithm for Boltzmann machines. *Cogn. Sci.* **9**, 147–169 (1985).
47. Li, C. Y., Poo, M. M. & Dan, Y. Burst spiking of a single cortical neuron modifies global brain state. *Science* **324**, 643–646 (2009).
48. Lisman, J. E. Bursts as a unit of neural information: making unreliable synapses reliable. *Trends Neurosci.* **20**, 38–43 (1997).
49. Omura, Y., Carvalho, M. M., Inokuchi, K. & Fukai, T. A lognormal recurrent network model for burst generation during hippocampal sharp waves. *J. Neurosci.* **35**, 14585–14601 (2015).
50. Izhikevich, E. M., Desai, N. S., Walcott, E. C. & Hoppensteadt, F. C. Bursts as a unit of neural information: selective communication via resonance. *Trends Neurosci.* **26**, 161–167 (2003).

Acknowledgements

We thank B. Shields for assistance with histology; D. Jin and R. Percy for assistance with morphological reconstructions; D. Otstot for animal breeding and genotyping; and L. Frank, J. Fitzgerald, J. Magee, and members of the Spruston lab for comments on the manuscript. This work was made possible by funding from the Howard Hughes Medical Institute.

Author contributions

D.L.H. conceived the project and designed the experiments in consultation with N.S. D.L.H. acquired and analyzed the in vitro electrophysiology data. D.L.H. acquired the in vivo electrophysiology data. D.L.H. and D.L. analyzed the in vivo electrophysiology data. B.S. and S.R. performed network simulations in consultation with D.L.H. and N.S. D.L.H. and N.S. wrote the manuscript with input from all co-authors.

Competing interests

The authors declare no competing interests.

Additional information

Supplementary information is available for this paper at <https://doi.org/10.1038/s41593-018-0172-7>.

Reprints and permissions information is available at www.nature.com/reprints.

Correspondence and requests for materials should be addressed to D.L.H. or N.S.

Publisher's note: Springer Nature remains neutral with regard to jurisdictional claims in published maps and institutional affiliations.

Methods

In vitro electrophysiology and analysis. Acute hippocampal brain slices were prepared from male and female (P23–P40) Wistar rats or transgenic mice (see below) according to methods approved by the Janella Institutional Animal Care and Use Committee. After animals were deeply anesthetized with isoflurane, 50 mL of chilled (4–8°C) sucrose cutting solution, consisting of (in mM) 215 sucrose, 2.5 KCl, 20 glucose, 26 NaHCO₃, 1.6 NaH₂PO₄, 1 CaCl₂, 4 MgCl₂, and 4 MgSO₄, was transcardially perfused. Following perfusion, mice were decapitated and the brain rapidly removed and placed into chilled sucrose cutting solution.

Whole hippocampi were dissected out of the brain, embedded in a preformed agar block (4% agar), cut into 400- μ m thick transverse sections on a Leica VT 1200s vibratome (Leica, Ltd., Germany), and transferred to a submersion incubation chamber containing room-temperature cutting solution. Once all the sections were transferred to the incubation chamber, the cutting solution was slowly exchanged with room-temperature artificial cerebrospinal fluid (ACSF) containing (in mM) 124 NaCl, 2.5 KCl, 10 glucose, 26 NaHCO₃, 1.0 NaH₂PO₄, 2.0 CaCl₂, and 1.0 MgCl₂. Both cutting and ACSF solutions were saturated with 95% O₂ and 5% CO₂ (pH 7.2–7.4) throughout slice preparation. The slices were incubated in ACSF for at least 1 h before recording, and then were transferred as needed to a submersion-type laminar-flow recording chamber, perfused with ACSF at 5 mL/min. Slices were stabilized within the recording chamber using a custom-made platinum harp with 2-mm spaced nylon fibers, specifically placed over the fimbria and subiculum, thereby minimally interfering with the DG-CA3 regions.

Whole-cell intracellular recordings were obtained using standard patch-clamp techniques in current-clamp mode, where the slice was visualized under infrared differential interference contrast (IR-DIC) optics with a Scientifica SliceScope (Scientifica, UK). The internal pipette solution for all recordings contained (in mM) 135 potassium-gluconate, 5 KCl, 1 CaCl₂, 0.1 EGTA-Na, 10 HEPES, 10 glucose, 5 MgATP, 0.4 Na₃GTP, and 0.5% biocytin, at pH 7.2 and 285–290 mOsm. To maximize cell health, synaptic connectivity, recording stability, and to obtain an unbiased sampling of CA3 pyramidal neurons, cells 100–150 μ m below the surface of the slice were blind-patched. The recording pipette resistance ranged from 4–6 M Ω . Bridge balance and capacitance compensation were monitored and manually adjusted (as needed) throughout each recording. Recordings with > 20% changes in input resistance were systematically excluded from analysis. Resting potential ranged from –79 to –58 mV. Maximal recording time after dissection was 6 h. Recording temperature was set to 32.0 \pm 0.1 °C using a TC-344A single-channel temperature controller (Warner Instruments, Inc., Hamden, CT, USA). All recordings were executed with a Dagan BVC-700 amplifier, filtered at 5 kHz and digitized at 20 kHz using an ITC-16 analog-to-digital converter (Instrutech Inc., Longmont, CO, USA), and analyzed using custom-written software for IgorPro (Wavemetrics Inc., Lake Oswego, OR, USA).

CA3 pyramidal neurons from the CA3a and CA3b subregions were identified as residing in stratum pyramidale, at least 100 μ m along the transverse axis from the distal edge of stratum lucidum and 100–200 μ m from the boundary of the two blades of the dentate gyrus. In all cases, a series of 500-ms current steps were applied to each cell, held at –60 \pm 1 mV, within 5–10 min after break-in, to determine the intrinsic properties of the cell being recorded. Cells were classified as regular-spiking or intrinsically bursting by the initial spike frequency resulting from a suprathreshold current injection 10–20% above rheobase for regular-spiking cells and at rheobase for intrinsically bursting cells. A host of physiological parameters in addition to the initial firing frequency, input resistance, and rheobase, were analyzed consistent with previous measurements²⁷. These include the after-depolarizing potential, the fast after-hyperpolarizing potential, and features of the first and second spike waveforms such as threshold, amplitude, full-width at half maximal amplitude, and maximum and minimum dV/dt . All measurements and analysis were performed using the IgorPro environment (Wavemetrics Inc., Lake Oswego, OR, USA) (<https://github.com/adamtaylor/DataPro>) and OriginPro software. All chemicals were purchased from Sigma-Aldrich (St. Louis, MO, USA) or Tocris (Bristol, UK).

Morphological reconstruction and analysis. Neurons were filled with biocytin for at least 20 min, and slices were then fixed for a minimum of 12–24 h with 4% paraformaldehyde after recording. Fixed brain slices were then washed in 1 \times PBS solution before staining. Biocytin staining was performed with vector PK4000 and SK4100 kits (Vector Laboratories, Burlingame, CA, USA). Digital images (z -stacks; 1- μ m intervals) of biocytin-stained neurons were obtained using semiautomated image acquisition in the Zeiss Zen software environment using a Zeiss Axioimager upright microscope equipped with a 100 \times (1.4 numerical aperture) objective and a Rolera-XR CCD camera (QImaging Inc., Surrey, BC, Canada). The z -stacks (TIFF format) were then imported into custom-written software for reconstruction and analysis.

Optogenetic-assisted circuit mapping of mossy fiber connectivity. To generate animals expressing channelrhodopsin in mossy-fiber axons, we selected a transgenic Cre-line that expressed high levels of Cre-recombinase in the majority of mature dentate granule cells, *Rbp4^{Cre}* (GENSAT, KL100). *Rbp4^{Cre}* mice were then crossed to the Ai32 (Channelrhodopsin2:YFP) reporter line⁵¹ (Jackson Labs

012569), the double-positive progeny (*Rbp4^{Cre}::Ai32*) of which were used for recordings. An identical strategy was employed for the *Pomc^{Cre}* (Jackson Labs # 005965) line, which is specific for newborn granule cells. Following a brief protocol to assess the intrinsic properties of the recorded neuron, optical stimulation of mossy fibers was achieved by full-field illumination through a 60 \times objective using 470-nm light with a pE-2 LED system (CoolLED Ltd. Andover, UK). Subthreshold mossy-fiber synaptic responses (EPSPs) were tuned to 5- to 10-mV amplitude with 1- to 5-mW/mm² light intensity with 1-ms pulse duration, paired-pulse (100-ms interpulse interval) stimulation. To analyze the cell-type-specific innervation from mossy fibers, all optically evoked synaptic responses were segregated according to the regular-spiking or bursting intrinsic properties of the cell, based on the criteria described above. The paired-pulse ratio (PPR; P2/P1) was calculated for each cell using the peak amplitude of the average synaptic response following optical stimulation. Response latency was measured following the first pulse from the onset of the optical pulse to the onset of the synaptic response, as defined by the first derivative of the voltage trace 1 s.d. above baseline. In a subset of experiments, the components of the synaptic response were pharmacologically segregated to determine the relative abundance of each component of ionotropic glutamatergic transmission. To segregate mossy-fiber responses from recurrent collateral-mediated synaptic responses, TTX (500 nM) and 4-AP (1 mM) or tetraethyl ammonium (TEA; 30 μ M) were perfused over the slice for 5 min before subsequent optical stimulation⁵². Pure mossy-fiber-mediated synaptic responses were then evoked with a 5-s, 8-mW/mm² optical pulse. Response amplitudes were measured as the peak depolarization within the duration of the light pulse. Responses were blocked with either NBQX (10 μ M) and d-APV (50 μ M) or DCG-IV (1 μ M) to confirm that they were indeed mossy-fiber synaptic responses.

Optogenetic activation of cholinergic fibers in vitro. To assay the cholinergic effects on cellular intrinsic properties and network dynamics, we used a transgenic approach in which *ChaT^{Cre}* mice (Jackson Labs # 006410) were crossed to the Ai32 (ChR2-YFP) reporter strain. The representative image of ChR2 expression in the hippocampus was acquired in a tiled manner at 63 \times magnification to visualize the thin cholinergic fibers. For in vitro experiments, acute brain slices were prepared from *ChaT^{Cre}::Ai32* mice, and cholinergic fibers were activated by full-field optical stimulation through a 10 \times objective. Three to five trains of pulsed optical stimulation (10-s duration, 5-Hz interpulse interval, 100-ms pulse duration) were used to build up a cholinergic tone in the slice before effects on cellular intrinsic properties could be observed.

In vivo electrophysiology and optogenetics. Adult animals (8–12 weeks old) were taken from their home cages and placed in an isoflurane chamber and lightly anesthetized. Once immobilized (but responsive to tail pinch), mice were headfixed in a stereotaxic alignment/recording system (Kopf instruments). CA3 was targeted with a 0.3- to 0.5-mm craniotomy (Dura remained intact) at coordinates –2.2 to –2.3 mm from bregma, 2.7 to 3.2 mm from the midline, and 1.5 to 2.5 mm from the dura surface. For the experiment conducted in Supplementary Fig. 7, an ipsilateral craniotomy targeting the CA1 region (–2.0 mm from bregma, 2.0 mm from the midline) was made for simultaneous CA3 + CA1 recordings. The CA1 electrode was then advanced downward (approximately 1–1.5 mm from the dura surface), collecting data at different depths. Single-unit recordings from CA3 were obtained using standard juxtacellular recording techniques. We used 1-mm OD, 0.7-mm ID quartz pipettes with resistances ranging from 10–15 M Ω ms targeted to stratum pyramidale, based on the presence of extracellular spiking. Isoflurane levels (1 \pm 0.4%) were continually adjusted to stabilize the sharp-wave brain state monitored on an oscilloscope and audio monitor. After obtaining a juxtacellular unit, the spontaneous occurrence of sharp-wave activity was recorded for 30–90 min. All recordings were executed with a Multiclamp 700B amplifier (axon instruments). Signals were filtered at 3–5 kHz using the amplifier's built-in Bessel filter and digitized (20 kHz) using an ITC-16 analog-to-digital converter (Instrutech). We acquired 20-s sweeps using custom-written software in the IgorPro environment (Wavemetrics Inc., Lake Oswego, OR, USA). To activate the cholinergic system in vivo, a craniotomy was drilled at +1 mm from bregma, just lateral to the midline fissure to avoid vasculature, targeting the medial septum. A 100- or 150- μ m-diameter fiber cannula (Thorlabs), coupled to a 470-nm LED light source (CoolLED, pE-4000), was then lowered to a depth of 3.0–3.5 mm from the cortical surface (dura removed). Trains of pulsed illumination were delivered (20- to 50-ms pulses, 100- to 200-ms interpulse interval, 8-s total duration). The response to cholinergic stimulation was measured in the CA3 region as a reduction of sharp-wave synchronization events detected in 4- to 20-Hz frequency band (see below).

Juxtacellular labeling, histology, and immunohistochemistry. To obtain morphological identification of juxtacellularly recorded neurons, biocytin was electroporated with multiple trains of current injection (2 Hz, 3–15 nA). Following electroporation (20–60 min), animals were transcardially perfused with 50 mL saline, followed by 4% paraformaldehyde fixative. Whole brains were dissected out and postfixed in 4% paraformaldehyde for 24–28 h, and then washed 3 \times in PBS. The brain was then cut into 100- to 150- μ m-thick sagittal sections and washed with PBS containing 0.3% Triton-X100 for 1 h at room temperature. Sections

were then incubated with fluorescent-tagged streptavidin diluted in PBS + 0.1% Triton-X100 at 4°C for 18–24 h. Streptavidin-conjugated neurons were visualized with an Alexa Fluor-conjugated secondary antibody (SA_Alexa Fluor-488 diluted at 1:500, Invitrogen S32354, or SA_Alexa Fluor-555 diluted at 1:1,000, Invitrogen S32355). In several cases, when neurons were labeled in the distal CA3 region, we performed immunostaining to confirm that recorded neurons were negative for the CA2 marker PCP4 or the inhibitory marker VGAT. Sections were incubated in blocking solution containing 5% normal goat serum, 2% bovine serum albumen, and 0.3% Triton-X100 for 2 h at room temperature. Sections were then incubated in primary antibody (rabbit anti-PCP4, Sigma, HPA005792) or (guinea pig anti-VGAT, Synaptic Systems, 131004) diluted at 1:200 in blocking solution with 0.3% Triton-X100 for 18–24 h at 4°C, followed by 1–3 h at room temperature. Sections were subsequently washed in 0.1% Triton-X100 for 10–20 min, three times. Sections were then incubated in secondary antibody solution (goat anti-rabbit Alexa Fluor-647, Invitrogen/Molecular Probes, A21245) diluted at 1:200 in blocking solution and 0.3% Triton-X100 for 2–4 h at room temperature (25°C). Sections were then washed again in 0.1% Triton-X100 for 10–20 min, three times. Stained sections were then rinsed in PBS, mounted on slides, and coverslipped with Vectashield hard-set mounting solution containing DAPI stain (Vector Labs, H1500). Recovered morphologies were then imaged on an inverted Zeiss 880 confocal microscope with a 63× objective to visualize the presence or absence of thorny excrescences on the proximal dendritic regions. We imposed strict criteria to determine whether thorny excrescences were present or absent for a given cell. We only designated a cell as athorny if the dendrites were filled to the most distal apical and basal processes and lacked multiheaded spiny protrusions along the proximal portion of the apical dendrite. For partially filled cells, we could not determine whether a cell was athorny, but if multiheaded spiny protrusions were clear along the proximal apical dendrite, the cell was designated as thorny.

In vivo data analysis. Wideband signals were digitally filtered in the bands 4–20 Hz, 100–250 Hz, and 0.3–3 kHz to extract the LFP (SW and ripple) and action potential (AP) waveforms. For each sweep in a recording session, we computed the value θ (θ)⁵³:

$$\theta_{AP} = \text{median} \left(\frac{|V_{AP}|}{0.6745} \right)$$

where V_{AP} is the wideband signal, highpass-filtered in the 0.3- to 3-kHz band. We set the threshold for detection of juxtacellular APs to $20 \times \theta_{AP}$. Given the decreasing amplitude of successive spikes in a burst, we used a variable threshold to reliably detect all APs comprising a burst: each time a spike was detected, we decreased the value of the threshold by $5 \times \theta_{AP}$ in the 20 ms following the AP (corresponding to a minimum intraburst frequency of 50 spikes/s). The threshold was decreased up to a minimum value of $5 \times \theta_{AP}$, reached after the fourth spike in a burst. A series of APs was identified as a burst if it comprised at least three action potentials of decreasing amplitude, occurring at a minimum rate of 50 spikes/s. The constraint on the decreasing amplitude was valid only for the first three spikes in a burst, to allow detection of bursts whose late spikes regained amplitude.

For each juxtacellular unit, we then computed the single-spike and complex-spike firing rates, defined as the number of single spikes and complex spikes (collapsed to a single event) divided by the total recording duration; the burst index, defined as the number of individual spikes in complex spikes divided by the total number of emitted spikes; and the mean number of individual spikes within a complex spike. We then performed principal component analysis of the above features for all juxtacellular recordings. Plotting the first two principal components relative to each other resulted in a distribution of observations, which were given a cluster assignment based on the local density of observations in two-dimensional PCA space (2D projection) based on previous methods⁵⁴. Additionally, we calculated the SW participation index as the fraction of SWs during which a given cell fired, relative to the total number of SWs in the recording.

Extracellular spikes were detected as downward crossings of a fixed threshold set at the value $-5 \times \theta_{AP}$. Threshold crossings occurring within a window of ± 4 ms from the peak of juxtacellular APs were discarded. Similarly to the burst-detection algorithm used for juxtacellular spikes, we identified putative bursts of extracellular APs by setting a minimum interspike interval of 50 Hz. However, to avoid classifying as bursts high-frequency volleys of APs originating from distinct single units, we applied the constraint of decreasing spike amplitude for all spikes in a burst. We then extracted the negative voltage peak; the FWHM (i.e., duration of the AP at half-amplitude); the positive voltage peaks before and after the negative peak; and spike asymmetry, defined as the time from baseline to negative peak divided by the time from negative peak to baseline.

To identify putative single units, we clustered the extracellular AP waveform features using KlustaKwik⁵⁵ and Matlab to merge clusters belonging to the same putative single unit. Briefly, from the AP features described above, we selected the features that displayed the best separation in feature space. The output clusters from KlustaKwik were then inspected to identify which putative clusters were most likely associated with single extracellular units. To this end, we inspected both the location of each cluster relative to the others in feature space (Supplementary Fig. 8) and its autocorrelogram. We merged those putative units that covered

overlapping areas in feature space, while still maintaining a minimum refractory period of 3 ms in the autocorrelogram. Given the relatively low firing rate of most cells in our recordings, 93% of units that met this criterion also displayed clear autocorrelation valleys, as shown in Supplementary Fig. 8. We did not make any attempt to split clusters and preferred to discard putative single units that were clearly contaminated and/or whose autocorrelogram did not meet our quality requirements. Moreover, to minimize clustering problems associated with the change in AP features of successive spikes in a burst (complex spikes), we only used the first spike in a burst and then assigned the remaining spikes in a burst to the appropriate single unit. Spikes that did not belong to any burst were classified as single spikes. Using these criteria, we identified 224 extracellular single units (with 1.3 units detected per recording on average).

To detect SW synchronization events, in each 20-s sweep in a recording session, we computed the value θ (θ), where V_{LFP} is the wideband signal filtered from 4–20 Hz.

$$\theta_{LFP} = \text{median} \left(\frac{|V_{LFP}|}{0.6745} \right)$$

We set the threshold for detection of SWs to $5 \times \theta_{LFP}$. For each detected SW, we extracted the time and voltage values of the peak, as well as the duration, defined as the window of time around the SW peak during which $V_{LFP} > \theta_{LFP}$. When juxtacellular or extracellular spikes occurred during the duration of a SW, a semisupervised procedure was used to confirm that the detected event was indeed a SW. We found this to be necessary when the juxtacellular signal-to-noise ratio was high enough to cause artifacts in the LFP trace, which at times would cross the threshold for SW detection. SW-triggered firing-rate histograms were constructed by taking the times of juxtacellular and extracellular APs in a 1-s-long window centered around each SW. The event times relative to the peak of the SW were binned (20 ms) and the number of events in each bin was divided by the product of the number of SWs and bin width to yield the firing rate.

To calculate confidence intervals, we generated surrogate event trains for all spikes, single spikes, and complex spikes. We then extracted interevent intervals (IEIs) as the time difference between two consecutive events, which were shuffled ($N = 1,000$) to generate a new set of IEIs. Surrogate event times were computed by cumulatively summing the shuffled IEIs. Notably, the first event time was chosen randomly, to ensure that the number of original events was preserved. This procedure maintains the original firing rate and distribution of IEIs, while removing the temporal structure that might be present in the original event times. Confidence intervals for the SW-triggered firing rates—for both original and surrogate event times—were computed according to⁵⁶. In the case of the original event times, we randomly selected half of the original SW-triggered trials $M = 10,000$ times, thus generating a surrogate dataset composed of original event times. For the shuffled event times, the surrogate dataset was composed of the $N = 1,000$ repetitions of the artificial event times triggered by the full set of SWs. In both cases, the event times were binned (20 ms) to compute artificial event counts. The distribution of event counts in each bin over the N repetitions was used to fit a Poisson distribution, whose first and 99th percentiles were taken as the lower and upper confidence bounds, respectively. The statistical significance between PSTHs was calculated for each 20-ms bin according to previously described methods⁵⁷.

Single-cell model. Individual neurons in the network are modeled as adaptive exponential integrate-and-fire units⁵⁸. The membrane potential V of a neuron (we temporarily neglect the cell index) is described by

$$C \frac{dV}{dt} = -g_L(V - E_L) + g_L \Delta t \left(\frac{V - V_T}{\Delta t} \right) - z + h$$

$$\tau_z \frac{dz}{dt} = a(V - E_L) - z$$

where h is the input current to the neuron, z is the adaptation current, g_L is the leak conductance, E_L is the leak reversal potential, V_T is the threshold for the exponential function, Δt is the slope factor, a is the adaptation coupling parameter, τ_z is the adaptation time constant, and C is the membrane capacitance. A spike is generated when the membrane potential crosses a threshold, $V > V_s$. Following the spike, V and z are reset according to the following rules;

$$V \leftarrow V_r$$

$$z \leftarrow z + b$$

Here V_r is the reset potential, and b is the spike-triggered adaptation. The parameters of the neurons were selected to reproduce the experimentally observed spiking properties of single cells in response to somatic current injections recorded in vitro. The parameters common to all cell types are $C = 281$ pF, $E_L = -70.6$ mV, $V_r = -50.4$ mV, $\Delta t = 2$ mV, and $V_s = V_T + 10$ mV. Additional parameters

specifying the unique intrinsic properties of the neurons are indicated in Supplementary Fig. 13.

Network model. The recurrent network is composed of $N=1,000$ neurons. Of these, N_E are excitatory neurons (80%), further subdivided into two types, a fraction p of athorny bursting cells, and $(1-p)$ thorny regular spiking cells. $N_I = N - N_E$ of the neurons are inhibitory (20%). Each cell in the network is labeled by a population index $A \in \{E, I\}$ and a cell index i within the population. Each excitatory neuron is assigned a preferred location on a ring, which could represent (for instance) its preferred firing location in a circular environment. The connection strength from neuron j in population B to neuron i in population A , denoted as J_{ij}^{AB} , is

$$J_{ij}^{AB} = \begin{cases} \frac{J^E W_{ij}}{N_E} & A = E, B = E \\ -\frac{J^I}{N_I} & A \in \{E, I\}, B = I \\ \frac{J^E}{N_E} & A = I, B = E \end{cases}$$

W_{ij} represents the distance-dependent connection strength between excitatory neurons on the ring

$$W_{ij} = \begin{cases} \exp\left(-\frac{|\theta_i^E - \theta_j^E|^2}{2\sigma^2}\right), & \text{with probability } c \\ 0, & \text{with probability } (1-c) \end{cases}$$

where $\theta_i^E \in [0, 1)$ is the preferred firing location of the i th excitatory neuron, and the preferred locations are regularly arranged on the ring. Note that these locations are chosen to be in the range $[0, 1)$. $|\cdot|$ denotes the distance on the ring. J^E , J^I , and J^{EI} are the connection strength within the excitatory neurons, the connection strength from the inhibitory neurons, and the connection strength from the excitatory neurons to the inhibitory neurons, respectively. The input to the i th neuron of the excitatory population is given by

$$h_i^E = I_i^E + \sum_j J_{ij}^{EE} u_j \sum_k \delta(t - t_{j,k}^E) + \sum_j J_{ij}^{EI} \sum_k \delta(t - t_{j,k}^I)$$

and the input to the i th neuron of the inhibitory population is given by

$$h_i^I = I_i^I + \sum_{j,B} J_{ij}^{IB} \sum_k \delta(t - t_{j,k}^B)$$

where $\delta(t)$ is the Dirac delta function, $t_{j,k}^B$ is the time of the k th spike of neuron j in population B . I_i^A is the external input to cell i in population A . For athorny (bursting) cells, $I = 0.25 I_0$; for thorny (regular spiking) cells and inhibitory cells, I is Gaussian white noise with 0 average and variance $\sigma^2 = 10^{-3} I_0^2$. I_0 modulates the overall strength of input current. The recurrent connections between excitatory cells are endowed with short-term synaptic plasticity dynamics

$$\frac{du_i}{dt} = -\frac{u_i}{\tau_f} + U(1 - u_i^-) \delta(t - t_i^E)$$

$$\frac{dx_i}{dt} = \frac{1 - x_i}{\tau_d} - u_i^+ x_i \delta(t - t_i^E)$$

where x_i is the fraction of available synaptic resources at excitatory synapses with presynaptic neuron i , and u_i is the average release probability. $u_i^+ = u_i^- + U(1 - u_i^-)$ is the fraction of available resources immediately after the arrival of the spike; u_i^- is the corresponding variable before the spike; and τ_f and τ_d are the facilitation and depression time constants, respectively. The network parameters used in our simulations are shown in Supplementary Fig. 14. The differential equations in the model are numerically solved using the Euler–Maruyama method with a time-step of 1 ms. The simulation results are unaltered for a smaller time-step of 0.1 ms (data not shown). The spiking pattern of a neuron in the network is classified as a single spike or a burst, according to the same criteria used for cells recorded in experiments (see above). vSWs are identified by clustering the spike times of thorny neurons. A vSW event is defined as synchronous spiking that contains at least 10 spikes within 1 ms. In addition, subsequent synchronous spiking events

need to be separated in time by at least 20 ms to be considered separate vSWs. The time of a vSW event is defined as the duration of the maximal population activity of thorny neurons. The onset of a sharp-wave event is defined as the time when population activity of thorny neurons, in 2-ms bins, first exceeds four spikes before the time of the vSW. The event size of a vSW for either one of the excitatory cell classes is defined as the number of peaks in the population-averaged activity within a time-window of 50 ms centered at the time of vSW, during which each activity peak should be composed of at least 4 spikes. The spatial location of a vSW event is defined as the average location of the activity of thorny cells during a vSW, estimated according to the first Fourier component of the spatial profile of activity, f_k , i.e., the activity of a neuron with preferred location $0 \leq \theta_k < 1$

$$Ae^{2\pi i \psi} = \sum_k f_k e^{2\pi i \theta_k}$$

where ψ is the resulting estimate of the SW spatial location. The spikes of the thorny and athorny neurons are aligned either to both the spatial location of the vSW and the time of vSW or to the onset of vSW. The PSTH is calculated for neurons within the activity ‘bump’ (neurons whose locations are within a distance $d = 0.15$ to the location of the vSW) or outside the activity bump (Supplementary Fig. 15).

Statistical analyses. No statistical methods were used to predetermine sample sizes, but our sample sizes are similar to those reported in previous publications^{18,27}. Data was collected in a blocked fashion, according to animal strain. Data collection and analysis were not performed blind to the conditions of the experiment. Generally, no data were excluded in this study. However, for in vitro electrophysiology, recordings with >20% changes in input resistance were systematically excluded from analysis. For juxtacellular labeling in vivo, we imposed strict criteria to determine whether thorny excrescences were present or absent for a given cell. We only designated a cell as athorny when the dendrites were filled to the most distal apical and basal processes and lacked multiheaded spiny protrusions along the proximal portion of the apical dendrite. For partially filled cells, we could not determine whether a cell was athorny, but if multiheaded spiny protrusions were clear along the proximal apical dendrite, the cell was designated as thorny. Statistical analyses were performed using OriginPro or Matlab. Normality was determined by a Shapiro–Wilk test at a significance level of 0.05 for parametric statistical comparisons, and all parametric tests were two-sided. Nonparametric two-sided tests were used for non-normal datasets.

Reporting Summary. Further information on experimental design is available in the Nature Research Reporting Summary linked to this article.

Data and code availability. Data is available through Figshare at <https://doi.org/10.25378/janelia.6189089> and <https://doi.org/10.25378/janelia.6189164>.

Electrophysiology data acquisition software is available at <https://github.com/JaneliaSciComp/DataPro>.

Morphological reconstruction software is available at <https://www.janelia.org/lab/spruston-lab/resources/shutu>.

Spike-sorting analysis software is available at <https://github.com/klusta-team/klustakwik>.

References

- Madisen, L. et al. A toolbox of Cre-dependent optogenetic transgenic mice for light-induced activation and silencing. *Nat. Neurosci.* **15**, 793–802 (2012).
- Petreaun, L., Mao, T., Sternson, S. M. & Svoboda, K. The subcellular organization of neocortical excitatory connections. *Nature* **457**, 1142–1145 (2009).
- Quiroga, R. Q., Nadasdy, Z. & Ben-Shaul, Y. Unsupervised spike detection and sorting with wavelets and superparamagnetic clustering. *Neural Comput.* **16**, 1661–1687 (2004).
- Rodriguez, A. & Laio, A. Machine learning. Clustering by fast search and find of density peaks. *Science* **344**, 1492–1496 (2014).
- Kadir, S. N., Goodman, D. F. & Harris, K. D. High-dimensional cluster analysis with the masked EM algorithm. *Neural Comput.* **26**, 2379–2394 (2014).
- Abeles, M. Quantification, smoothing, and confidence limits for single-units’ histograms. *J. Neurosci. Methods* **5**, 317–325 (1982).
- Dörrscheidt, G. H. The statistical significance of the peristimulus time histogram (PSTH). *Brain Res.* **220**, 397–401 (1981).
- Brette, R. & Gerstner, W. Adaptive exponential integrate-and-fire model as an effective description of neuronal activity. *J. Neurophysiol.* **94**, 3637–3642 (2005).

Reporting Summary

Nature Research wishes to improve the reproducibility of the work that we publish. This form provides structure for consistency and transparency in reporting. For further information on Nature Research policies, see [Authors & Referees](#) and the [Editorial Policy Checklist](#).

Statistical parameters

When statistical analyses are reported, confirm that the following items are present in the relevant location (e.g. figure legend, table legend, main text, or Methods section).

n/a Confirmed

- The exact sample size (n) for each experimental group/condition, given as a discrete number and unit of measurement
- An indication of whether measurements were taken from distinct samples or whether the same sample was measured repeatedly
- The statistical test(s) used AND whether they are one- or two-sided
Only common tests should be described solely by name; describe more complex techniques in the Methods section.
- A description of all covariates tested
- A description of any assumptions or corrections, such as tests of normality and adjustment for multiple comparisons
- A full description of the statistics including central tendency (e.g. means) or other basic estimates (e.g. regression coefficient) AND variation (e.g. standard deviation) or associated estimates of uncertainty (e.g. confidence intervals)
- For null hypothesis testing, the test statistic (e.g. F , t , r) with confidence intervals, effect sizes, degrees of freedom and P value noted
Give P values as exact values whenever suitable.
- For Bayesian analysis, information on the choice of priors and Markov chain Monte Carlo settings
- For hierarchical and complex designs, identification of the appropriate level for tests and full reporting of outcomes
- Estimates of effect sizes (e.g. Cohen's d , Pearson's r), indicating how they were calculated
- Clearly defined error bars
State explicitly what error bars represent (e.g. SD, SE, CI)

Our web collection on [statistics for biologists](#) may be useful.

Software and code

Policy information about [availability of computer code](#)

Data collection

Electrophysiology data was collected with custom written IgorPro software available at; (<https://github.com/adamtaylor/DataPro>). Morphological reconstructions were performed with custom written code available at; (<https://www.janelia.org/lab/spruston-lab/resources/shutu>).

Data analysis

Data was analyzed with OriginPro or MATLAB software. Spike sorting analysis software is available at (<https://github.com/klusta-team/klustakwik>).

For manuscripts utilizing custom algorithms or software that are central to the research but not yet described in published literature, software must be made available to editors/reviewers upon request. We strongly encourage code deposition in a community repository (e.g. GitHub). See the Nature Research [guidelines for submitting code & software](#) for further information.

Data

Policy information about [availability of data](#)

All manuscripts must include a [data availability statement](#). This statement should provide the following information, where applicable:

- Accession codes, unique identifiers, or web links for publicly available datasets
- A list of figures that have associated raw data
- A description of any restrictions on data availability

Data is available through Figshare at: (<https://doi.org/10.25378/janelia.6189089>), and <https://doi.org/10.25378/janelia.6189164>).

Field-specific reporting

Please select the best fit for your research. If you are not sure, read the appropriate sections before making your selection.

Life sciences Behavioural & social sciences Ecological, evolutionary & environmental sciences

For a reference copy of the document with all sections, see nature.com/authors/policies/ReportingSummary-flat.pdf

Life sciences study design

All studies must disclose on these points even when the disclosure is negative.

Sample size	No statistical methods were used to predetermine sample sizes. Sample sizes were chosen to be similar to those reported in previous publications.
Data exclusions	Generally, no data were excluded in this study. However, for in vitro electrophysiology, recordings with >20% changes in input resistance were systematically excluded from analysis. For juxtacellular labeling in vivo, we imposed strict and principled criteria to determine whether thorny excrescences were present or absent for a given cell. We only designated a cell to be athorny if the dendrites were filled to the most distal apical and basal processes and lacked multi-headed spiny protrusions along the proximal portion of the apical dendrite. For partially filled cells, we could not determine if a cell was athorny, however if multi-headed spiny protrusions were clear along the proximal apical dendrite, the cell was designated as thorny.
Replication	All experiments in this study were reliably reproduced. However, there is a non-zero failure rate associated with obtaining whole-cell patch clamp recordings in-vitro (brain slices), and juxtacellular recordings in-vivo. This rate is largely based on the skill level of the experimenter and in this study was approximately 10-20%.
Randomization	All samples were allocated to groups based on animal strain (i.e. Wild-type or transgenic)
Blinding	Experimenters were not blinded to group identity (i.e. animal strain). However, data was collected in the most unbiased manner possible where whole-cell recordings were obtained in brain slices by blind-patch technique, and juxtacellular recordings were acquired blindly in-vivo.

Reporting for specific materials, systems and methods

Materials & experimental systems

n/a	Included in the study
<input checked="" type="checkbox"/>	<input type="checkbox"/> Unique biological materials
<input type="checkbox"/>	<input checked="" type="checkbox"/> Antibodies
<input checked="" type="checkbox"/>	<input type="checkbox"/> Eukaryotic cell lines
<input checked="" type="checkbox"/>	<input type="checkbox"/> Palaeontology
<input type="checkbox"/>	<input checked="" type="checkbox"/> Animals and other organisms
<input checked="" type="checkbox"/>	<input type="checkbox"/> Human research participants

Methods

n/a	Included in the study
<input checked="" type="checkbox"/>	<input type="checkbox"/> ChIP-seq
<input checked="" type="checkbox"/>	<input type="checkbox"/> Flow cytometry
<input checked="" type="checkbox"/>	<input type="checkbox"/> MRI-based neuroimaging

Antibodies

Antibodies used

Primary antibodies;
 Rabbit anti-PCP4 (Sigma, HPA005792, 1:200, lot # D105912)
 Guinea pig anti-VGAT (Synaptic Systems, 131004, 1:200, lot # 131004/18)

Secondary antibodies;

SA_AlexaFluor 488 (Invitrogen, S32354, 1:500)
 SA_AlexaFluor 555 (Invitrogen, S32355, 1:1000)
 SA_AlexaFluor 647 (Invitrogen, A21245, 1:200)
 (we did not track lot # information for secondary antibodies)

Validation

All antibodies used in this study are commercially available and knockout validated by the vendor and by data in our study (see vendor website for product numbers listed below).

Animals and other organisms

Policy information about [studies involving animals](#); [ARRIVE guidelines](#) recommended for reporting animal research

Laboratory animals

All data in our study was collected from both male and female rats or transgenic mice (see below for strain information). For in vitro electrophysiology, P23-40 animals were used. For in vivo electrophysiology, animals 8-12 weeks were used.

Rat strains;
 Wild-type, Wistar

Mouse strains;
 Rbp4-cre, GENSAT, KL100
 Pomc1-cre, Jackson Labs, 005965
 ChaT-cre, Jackson Labs, 006410
 Ai32, Jackson Labs, 012569

Wild animals

n/a

Field-collected samples

n/a